A STUDY OF THE REACTIONS ^{9}Be(p,α) AND ^{9}Be(p,d) AT LOW ENERGIES

Thesis by

Arnold John Sierk

In Partial Fulfillment of the Requirements

for the Degree of

Doctor of Philosophy

California Institute of Technology

Pasadena, California

1973

(Submitted November 10, 1972)

ACKNOWLEDGMENTS

I wish to thank the faculty and staff of the Kellogg Radiation Laboratory for the stimulating and friendly environment they have provided. My association with Professor T. A. Tombrello has been especially rewarding.

I am grateful for the advice given by Professor C. A. Barnes on the operation of the 700 KeV Van de Graaff. Mrs. B. A. Zimmerman has given valuable computing assistance.

I appreciate the financial assistance given me by the National Science Foundation, the California Institute of Technology, and the Fannie and John Hertz Foundation. This research was supported in part by the National Science Foundation (GP-28027).

ABSTRACT

Cross sections for the $^{9}Be(p,d)$ and (p,α) reactions have been measured for proton lab energies of 30 to 700 KeV. Angular distributions were measured for energies of 100 to 600 KeV. Absolute normalization of the cross sections was done by measuring cross sections for Rutherford scattered alpha particles. The maximum cross sections observed at the 330 KeV $J^{\pi} = 1^{-}$ resonance were (360 ± 20) mb for (p,α) and (470 ± 30) mb for (p,d). The value of $S_{cm}(E=0)$ for the combined cross sections was estimated to be $(35\ ^{-15}_{+45})$ MeV-barn.

The reaction data were interpreted in terms of an R-matrix compound nucleus model. There were no obvious effects due to direct reactions. The low energy behavior of the cross sections was fitted by using three ^{10}B resonance levels; a $J^{\pi} = 2^{+}$ level at -20 KeV (cm), a 1^{-} level at 310 KeV and a 1^{+} level at 410 KeV.

TABLE OF CONTENTS

I. INTRODUCTION

The exothermic reactions $^{9}Be(p,\alpha)^{6}Li$ (Q = 2.13 MeV) and $^{9}Be(p,d)^{8}Be \rightarrow 2\alpha$ (Q = .56 MeV) have unusually large cross sections at low proton energies. These reactions show a strong resonance in total cross section at about 330 KeV proton lab energy (Thomas, et al, 1949). This resonance is due to a $J^{\pi} = 1^{-}$ level in the ^{10}B compound nucleus (Lauritsen and Ajzenberg-Selove, 1966). Despite a higher Coulomb barrier, the cross sections are significantly higher, at energies greater than 200 KeV, than those of most reactions considered for possible fusion reactors (McNally, 1971). For this reason, and because all the reaction products are charged, the reactions have been considered promising for use in a power generating nuclear fusion reactor (Elwyn, et al, 1971; McNally, 1971).

Knowledge of the low energy cross sections for these reactions is also important for calculations of element nucleosynthesis and light element abundances in stars (Reeves and Audouze, 1968; Audouze, 1970; Wallerstein and Conti, 1969; Wagoner, 1969). Although the elemental abundances resulting from these processes are quite sensitive to the cross sections, the cross sections are not well known.

The magnitude of these cross sections at low energy was believed to be partly due to the presence of a very loosely bound neutron (1.67 MeV separation energy, Lauritsen and Ajzenberg-Selove, 1966) which extends quite far into the Coulomb barrier to incoming protons. It was also expected that direct reaction processes might contribute significantly.

This experimental study had two major objectives. First, to accurately measure the total reaction cross sections from as low an energy as possible to about 700 KeV, well above the energy where earlier work appeared quite accurate (Weber, et al, 1955; Neuendorffer, et al, 1951). Second, to measure angular distributions of reaction products over the entire energy range, especially at the 330 KeV resonance, which had been measured as nearly isotropic by Mozer (1956), although some asymmetry had been suggested by the deuteron polarization measurements of Robinson (1967). In addition, the existence and character of a possible resonance at 470 KeV (proton lab energy) (Lauritsen and Ajzenberg-Selove, 1966) were to be investigated.

I shall discuss the experimental apparatus and methods in Section II, present experimental results in Section III, and estimate random errors in Section IV. Section V contains a discussion of a theoretical analysis of the data using a combination of direct reaction and R-matrix theory.

II. EXPERIMENTAL PROCEDURE

The 700 KeV Van de Graaff electrostatic generator of the Kellogg Radiation Laboratory was used to produce a hydrogen ion beam which was energy analyzed by a 90^{o} bending magnet system (Davids, 1968). The bending magnet was calibrated by observing the gamma ray yield from the following reactions (Lauritsen and Ajzenberg-Selove, 1966):

1) The 163 KeV resonance in $^{11}B(p,\gamma)$ with H^+ and HH^+ beams
2) The 227, 340 and 483 KeV resonances in the $^{19}F(p,\alpha\gamma)$ reaction with the H^+ beam.

For the study of the $^{9}Be(p,x)$ reactions, three ion species were used. HHH^+ was used for proton energies from 30 to 70 KeV, HH^+ from 60 to 210 KeV, and H^+ from 140 to 700 KeV.

The ion beam was defined vertically and horizontally by two sets of slits about 30 cm apart, between the energy regulation slits and the target, and about 30 cm from both. Immediately beyond the last slit was a larger slit to remove ions scattered from the slit edges. This slit was biased to -300 volts to suppress electrons emitted from the previous slits. The targets were mounted on a rod on the vertical axis of a 30 cm diameter cylindrical scattering chamber. This rod could be rotated and moved vertically to position the targets. For solid target measurements, beam charge was collected from this insulated target rod, which was biased at +140 volts. When thin targets were used, the target was grounded and beam current was collected from a 5×15 cm cylindrical Faraday cup, biased at +140 volts, placed 30 cm beyond the target. Between the target and the cup was an electron suppressor

ring, biased to -300 volts.

The system was pumped by an LN_2 trapped oil diffusion pump located near the first set of slits and by a 4" LN_2 sorption trap located under the Faraday cup and electron suppressor ring. The pressure in the scattering chamber was monitored by a Phillips discharge gauge, and was less than 1×10^{-5} torr during all experimental runs.

Two silicon surface barrier particle detectors were located in the scattering chamber. These were mounted on separate rotating arms at a distance of 8.5 cm from the axis of the chamber. The solid angle of the detectors was about 10^{-3} steradians, defined by a 3 mm circular hole in a tantalum disc in front of each detector. When properly biased the response of these detectors to an entering particle is a pulse of total charge proportional to the particle energy. The detectors were attached to Tennelec 100-A low noise preamplifiers and a Tennelec 901-RM bias supply and preamp power supply. The output of the preamp and detector circuit is a pulse with voltage proportional to the particle energy. The pulses from the detectors were simultaneously stored in two 100 channel quadrants of an RIDL 400-channel pulse height analyzer, using a homemade summing amplifier and an RIDL 30-17 signal routing system.

The beam current and integrated charge were measured with an Eldorado CI-110 current integrator.

Two types of targets were used. For energies of 30 to 210 KeV solid targets of 6 micrograms/cm^2 of ^9Be vacuum evaporated onto a .25 mm tantalum backing were used. With these targets, the detectors were

protected from elastic scattered protons by 6250Å commercial nickel foils, which completely stop protons with energies of less than about 150 KeV. For higher energies, thin self-supporting targets were used. These were made from 15 micrograms/cm^2 of ^{9}Be vacuum evaporated onto commercial 5 or 10 micrograms/cm^2 ^{12}C foils, which were then mounted on tantalum frames with 1 cm diameter apertures. The detectors were not masked with nickel foils when these targets were used.

All excitation function measurements were normalized to the value at a single energy, with absolute normalization being made by comparing reaction counting rates to Rutherford alpha particle scattering data. Angular distributions were all normalized to the value at $\theta_{cm} = 90^o$.

III. EXPERIMENTAL RESULTS

In this section the experimental results are presented and various corrections explained.

A. Angular Distributions

The angular distributions at 110 and 140 KeV were measured using solid targets, with a single detector being moved over the range $\theta_{lab} = 60^{o}$ to 160^{o}. The raw counting rates were corrected for $d\sigma_{cm}/d\sigma_{lab}$ and for $d\Omega(\theta)$ (Appendix, Parts A and C). All other angular distributions were taken with two detectors and thin targets. One detector was moved over the range from $\theta_{lab} = 30^{o}$ to 105^{o} with the reaction products passing through the target, and the other was used for $\theta_{lab} = 60^{o}$ to 160^{o} (backscattering). These data had the same corrections applied to give the results presented here. In Figures 1-3 the angular distributions for deuterons are given; those for alphas are shown in Figures 4-6. At energies above 400 KeV and angles greater than 90^{o}, the deuteron and ^{6}Li counts in the analyzer were not resolvable. It was necessary to subtract from the combined counts an estimated ^{6}Li count calculated from the observed alpha count rate at $\pi - \theta_{cm}$.

Results worth noting include the very large $P_1(\cos\theta)$ term in the (p,d) distribution at very low energies, the smaller, but still appreciable asymmetry in the (p,α) results at about 200 KeV, the change in sign of the deuteron asymmetry at about 200 KeV, the large $P_2(\cos\theta)$ component of the deuteron distribution at both the 330 and 470 KeV resonances and the large asymmetry of the (p,α) cross section at the 470 KeV resonance.

The angular distributions have been approximated by a series of Legendre polynomials. In Figures 7 and 8 the ratios of the $n = 1$ and 2 coefficients to the isotropic part of $d\sigma/d\Omega$ are plotted.

Values of these ratios for energies between 110 and 600 KeV were obtained from the angular distributions shown in Figures 1 to 6. Values below 110 KeV were obtained from the relative deuteron and alpha counting rates in detectors placed at different angles. The (p,α) cross section was assumed isotropic, and the (p,d) assumed to have only P_o and P_1 dependence, for those points below 110 KeV. For energies above 600 KeV, the data for (p,α) came from comparing alpha and ^{6}Li counting rates in detectors at different angles. The (p,d) points came from comparison of d to α and ^{6}Li data from the same detector. Both distributions were assumed to have only P_o and P_1 components for energies of 600 to 700 KeV. Besides definitely confirming the existence of the 470 KeV resonance, these results also support the existence of a previously reported anomaly at about 680 KeV (Neuendorffer et al, 1951; Thomas, et al, 1949; Lauritsen and Ajzenberg-Selove, 1966).

B. Excitation Functions

The raw data for the excitation functions were the counting rates in detectors placed at $\theta_{lab} = 85^o$ or 90^o. The results were corrected for $d\sigma_{cm}/d\sigma_{lab}$ (Appendix, Part A) and corrected to $\theta_{cm} = 90^o$ using the $P_1(\cos\theta)$ coefficients from Figures 7 and 8. $\sigma(E)$ was calculated from $\sigma = 4\pi(1 - \frac{1}{2} a_o/a_2)^{-1} (d\sigma/d\Omega)_{\theta_{cm}=90^o}$, where a_o and a_2 are

the coefficients of the Legendre polynomials in the series expansion for $d\sigma/d\Omega(\theta)$. The results were also corrected for effective charge collection, thickness effects and surface contaminant buildup for low energy runs (Appendix, Parts D, E, and F). The solid target data were normalized to the thin target results over the energy range 140 to 210 KeV (see Figures 9 and 10).

C. Normalization of Excitation Functions Using Rutherford Scattering

The absolute cross section normalization was performed by comparing reaction counting rates to Rutherford cross sections for elastically scattered alpha particles. With the target and a detector fixed, the target was bombarded with alpha particles with energies of 400 to 630 KeV, then the (p,α) reaction cross section was measured with 310 to 360 KeV protons. For the alpha energies mentioned, and for $\theta_{lab} = 80^{o}$, the elastic scattering peaks from the ^{9}Be and the ^{12}C in the target were well resolved. The raw counting rates for the scattering from the beryllium were multiplied by E^2, where E is the average energy of the alphas in the beryllium target layer. They were also corrected for the equilibrium charge state of alphas at the energy at which they left the target (Armstrong, et al, 1966). This factor converts measured electrical current into particle current. The energy that the particles lost in the target was computed by using the previously measured target thicknesses and published dE/dx values (Williamson, et al, 1966). The Rutherford scattering data, with these two corrections, are plotted in Figure 11. They lie nearly on a straight line, as they should for Rutherford scattering. As a further check that the scattering was pure

Rutherford, a $\csc^4(\theta_{cm}/2)$ dependence of the scattering was verified, within ± 2%, for lab angles of 60^o to 130^o, at energies of 400 and 550 KeV. The measured value of $(2.59 \pm .07) \times 10^3$ MeV^2-counts/particle-microcoulomb corresponds to a theoretical value of $E^2(d\sigma/d\Omega)_R$ = 450 ± 15 millibarn-MeV^2. The values of the 330 KeV and $\theta_{cm} = 90^o$ reaction counting rates were 160 ± 3 counts/particle-μC for (p,α) and 195 ± 5 counts/particle-μC for (p,d) . With a 10% correction to the (p,d) value due to the $P_2(\cos\theta)$ term in the angular distribution, the resulting maximum cross sections are $\sigma(p,\alpha)$ = 360 ± 20 mbarn , and $\sigma(p,d)$ = 470 ± 30 mbarn.

D. Astrophysical S Function

In calculations of astrophysical processes, the function $S(E) = E_{cm}(\sigma_\alpha + \sigma_d)\exp(b/E_{cm}^{1/2})$, where $b = \pi Z_1 Z_2 e^2\sqrt{2m}/\hbar$ is more commonly tabulated than σ (see, for example, Fowler, et al, 1967). The S function for the destruction of ^{9}Be, using the sum of the (p,d) and (p,α) cross sections of Figures 9 and 10 is presented in Figure 12. The estimated value of S(0) is $(35\ ^{-15}_{+45})$ MeV-barn (see Section V, Part C).

IV. RANDOM ERRORS

This section includes an estimate of random uncertainties from various parts of the experiment. These estimates are necessarily partly subjective, with some checks on accuracy being provided by frequent re-measurement of many data points. When a result is quoted as $x \pm \Delta x$, Δx refers to an estimated σ, i.e., the true value of x is expected with roughly 70% probability to lie within Δx of x.

A. Statistical Counting Errors

For energies greater than 70 KeV, all measurements have statistical uncertainties $(\sqrt{n}/n)$ of less than 2%. For the very lowest energies measured, the counting rates were low enough to increase counting errors to ±10%.

B. Current Measurement and Charge Collection

The current integrator was checked by integrating a known current source over various meter ranges and integration times. The accuracy was found to be at least ±0.5% over all current and charge ranges used in these measurements.

The biasing of the Faraday cup was varied from +70 volts to +450 volts and that of the suppressor from -300 to -1000 volts for H^+ and He^+ beams of energies from 250 to 600 KeV with no observable effect (<1%) on the measured current. Currents measured from the solid targets were compared to those measured at the cup with the target removed for several energies, and found to agree within 1%.

The estimated random error in measured charge due to all causes is ±1%.

C. Effective Charge Collection

At low energies, when the thin target was used, the charge measured relative to the charge collected when the target was removed is accurate to ±1% (Appendix, Part D).

D. Beam Energy

The incident proton beam energy was determined by the method described in Section II to better than ±0.3%. The energies of the incoming alpha particles used in the Rutherford scattering were uncertain by ±1%.

E. Alpha Particle Average Charge

The thicknesses of the 50 KeV thick targets were measured by recording the shifts in energy of an elastically scattered alpha peak caused by placing a target in front of a detector. Thicknesses were determined to ±5%. The final energy of the alpha particles was thus known to approximately ±1.5%. The data of Armstrong, et al (1966) are accurate to ±2%, so the average charge state of the exiting alpha particles was known to ±2.5%.

F. Energy of the Alpha Particles in the ^{9}Be Target Layer

The value of E^2 used in multiplying the counting rate of elastically scattered alphas was determined from the known relative thickness of ^{9}Be to ^{12}C in the target (obtained from counting the two

peaks), the total energy loss through a target as measured above and the tabulated dE/dx values for ^{9}Be and ^{12}C (Williamson, et al, 1966). E^2 is estimated to be known within ±2%.

G. Lab Angle of Detector

The lab angle of the detector is known to ±0.5°. At $\theta_{lab} = 80^{o}$ this produces an uncertainty in the theoretical Rutherford cross section of ±3%.

H. Normalization of Detector Solid Angle and Target Thickness

The total uncertainty in converting counting rates to absolute cross sections by means of the Rutherford scattering measurements is estimated by incoherently summing the errors from Parts B and D to G. This uncertainty is ±4.5%.

I. (p,α) Reaction Cross Section at 330 KeV

The unnormalized counting rate of reaction products at the peak of the 330 KeV resonance was determined to ±2%, so the absolute cross section for $^{9}Be(p,\alpha)^{6}Li$ at this energy is known within ±5%.

J. (p,d) Reaction Cross Section at 330 KeV

All deuteron counting rates were normalized with respect to alpha counting rates in the same detector. The total cross sections included a correction from $\theta_{cm} = 90^{o}$ data whenever a $P_2(\cos\theta)$ term was present. The relative uncertainty of (p,d) cross sections with respect to (p,α) is estimated to be ±2%. Thus, the absolute cross section for (p,d) is uncertain by ±6%.

K. Angular Distributions

The principal uncertainties in the angular distributions arose from:

1) Uncertainty of $\pm 0.5^{\circ}$ in θ_{lab} ; this results in 0-2% uncertainty in $d\sigma/d\Omega$, where the larger value is for the most asymmetric distributions.

2) Uncertainty in the position of the beam spot with respect to the axis of the scattering chamber. This gives rise to a systematic (with angle) error of uncertain magnitude. This would affect $d\sigma/d\Omega$ by at most ±1% (Appendix, Part C).

3) At low angles, the peak due to deuterons from the (p,d) reaction began to include some counts due to elastically scattered protons. This effect varies with energy and produced errors of up to ±5% in $d\sigma/d\Omega$ at $\theta_{lab} = 30^{\circ}$.

4) At high angles and energies, the deuteron angular distribution obtained from subtraction of an assumed $d\sigma/d\Omega$ for ^{6}Li from the combined rate (Section III, Part A) was uncertain by as much as ±5%, again depending on energy and angle. The cumulative effect of these errors is included in the error bars of Figures 1-6.

L. Excitation Functions--Thin Targets

The estimated uncertainty for $\sigma(p,\alpha)$ with respect to its value at 330 KeV, due to statistics, current integration, charge collection and target thickness is ±3% for energies above 230 KeV. For energies near 150 KeV, the uncertainty reaches a maximum of about ±5%.

As mentioned earlier, the deuteron excitation function was measured relative to the alpha and had a maximum relative uncertainty of ±2%.

M. Excitation Functions--Solid Targets

There is an estimated uncertainty of ±3% in the normalization of the thick target counting rates with respect to thin target rates at the same energies (Figures 9 and 10).

The primary uncertainties came from correcting for target thickness and contaminant buildup during a run. The target thickness was estimated by comparing counting rates from the thick target with those from thin targets of known thicknesses at the same energies. This gave the thickness of ^{9}Be on the solid targets in the beam direction as 10 ± 1.5 $\mu g/cm^2$. This uncertainty in thickness, along with the uncertainties introduced by the approximations in the Appendix, results in a varying uncertainty in the correction factor applied to the low energy counting rates. The maximum uncertainty due to this cause is 20% at 30 KeV, with less at energies above 30 KeV. The correction for deposition (Appendix, Part D) has an uncertainty varying from ±10% at 30 KeV to less than 1% at 150 KeV.

N. S Function

The S function has roughly the same uncertainty as σ, except at very low energies. Due to the exponential involved in S, an energy uncertainty of ±1 KeV at 50 KeV results in an uncertainty in S of ±20%.

The effects discussed in Parts L and M are included in the error bars of Figures 9-10, and those from L, M and N in Figure 12.

V. THEORETICAL ANALYSIS

Differential cross sections have been determined using T-matrix elements calculated from direct reaction and R-matrix theory. R-matrix theory (Lane and Thomas, 1958) provides a relatively simple parametrization of resonant and compound nucleus processes, which are confined to a restricted region of interaction. Because the weakly bound neutron in ^{9}Be extends far outside the usual R-matrix interaction radius into the proton Coulomb barrier, it was thought possible that direct reaction processes (not simply describable in the R-matrix framework) might contribute significantly to the low energy cross sections and angular distributions.

A. Direct Reaction Amplitude

Following Thomas (1955), we separate the T-matrix elements:

$$T_{cc'}^{J^\pi} = T^{\text{direct}} + T^{\text{comp.nucl.}}$$

$T^{c.n.}$ is formed from an R-matrix, and T^{direct} from the matrix element of the external (outside the interaction radius) neutron-proton potential between the initial and final scattered states:

$$T^{\text{direct}} = i/\hbar \int \phi_p^* \, V^{\text{ext}} \, \psi_{\text{out}} \, dx \, .$$

The integration is over all configuration space external to the interaction region of the R-matrix theory. ψ_{out} is the solution to the complete Hamiltonian of the system having the boundary conditions of only an incoming wave in the d (or α) channel at large distances.

ϕ_p is the solution to the partial Hamiltonian (with V^{ext} removed) with the boundary condition of only an outgoing wave in the proton channel. These states are time-reversed from the usual definition (Thomas, 1955).

In evaluating T^{direct}, the following approximations were used:

(1) Both ϕ_p and ψ_{out} were assumed to be pure Coulomb waves; this includes the DWBA of replacing ψ_{out} with ϕ_{out} (the solution to the partial Hamiltonian with the same boundary conditions as ψ_{out}) and assuming that the nuclear phase shifts are negligible compared to the Coulomb phase shifts.

(2) The electrical polarization of the outgoing particles by their mutual electric fields and the d-wave part of the deuteron wave function were ignored.

(3) The neutron-proton potential was approximated by a zero-range potential; if $U_d(r_{np})$ is the deuteron ground-state wave function, $V^{ext}(r_{np})\ U_d(r_{np}) = A_1\delta^3(r_{np})$.

(4) The proton only interacts with a single neutron bound to a ^{8}Be core in a pure p-wave state with a wave function in the external region of

$$iN_1\ Y_1^m(\Omega_n)\ \exp(-\beta_1 r_n)\ ,$$

where β_1 is the decay constant associated with the 1.67 MeV neutron separation energy of ^{9}Be.

(5) For the (p,α) calculation, the wave function of the alpha particle in the ^{8}Be core was approximated by $N_2\ \exp(-\beta_2 r)$ in the external region. The ^{6}Li nucleus was assumed to be

formed of a deuteron and an alpha particle bound in an s-wave state. The ^{6}Li internal wave function was replaced by a delta function of the variable $(\vec{r}_d - \vec{r}_\alpha)$. β_2 was arbitrarily chosen to be the inverse of the interaction radius of ^{9}Be.

The above approximations were made to simplify the analytic form of the integrals in T^{direct}.

The initial and final channel wave functions and the expression for T^{direct} are given in Appendix G. T^{direct} contains various angular momentum conservation and parity selection factors, and a radial integral of Coulomb and exponential functions. The only free parameter is an overall strength factor multiplying T^{direct}. This parameter includes the n-p interaction strength A_1, and the amplitudes of the exponential wave function tails, N_1 and N_2 .

B. Compound Nucleus Amplitude

The compound nucleus contribution to the transition matrix was approximated by including three distinct R-matrix pole terms. The three channel interaction radii and the reduced width amplitudes and energies of the poles were parameters which were varied to fit the experimental cross sections. The terms included were:

1. a $J^\pi = 1^-$ level at 310 KeV (cm)
2. a $J^\pi = 2^+$ level at -20 KeV
3. a $J^\pi = 1^+$ level at 410 KeV.

Level #1 is the 330 KeV (lab) resonance which had been identified

previously (Lauritsen and Ajzenberg-Selove, 1966). Level #2 has been seen in $^{9}Be(^{3}He,d)$ and (d,n) reactions and in alpha scattering from ^{6}Li in the past (ibid). Level #3 is the resonance which had been previously seen in the (p,d) channel at 470 KeV (lab), but which had no J^{π} assignment (Thomas, et al, 1949).

C. Comparison to Experimental Data

The theoretical parameters were determined in four stages:

1) The 50 to 400 KeV cross section was approximated using a single 1^- pole in the R-matrix.
2) The direct interaction was included with the first pole.
3) The effect of an additional R-matrix pole 20 KeV below proton threshold was included.
4) A third pole at higher energy was introduced.

Because of the number of parameters involved in the interaction of several broad resonances, it is not possible to determine a unique fit to the experimental cross sections and angular distributions. For the same reason, a "best fit" was not attempted. The goal was to explain the important qualitative characteristics of the results.

1). The 330 KeV Level. The 330 KeV resonance, the most striking feature of the low energy cross sections, was fitted by a 1^- level in the ^{10}B compound nucleus. The magnitudes of the cross sections at the resonance and at a lab energy of 50 to 100 KeV were the determining factors in making the fit. It was necessary to use interaction radii about 2 to 3 fm greater than those calculated from standard nuclear

radii to fit the very high and broad cross section curve of this resonance. It is possible that the large neutron average radius in ^{9}Be causes significant compound nucleus formation rates at quite large radii.

This state is necessarily of negative parity because of the formation by s-wave protons. A $J^{\pi} = 2^{-}$ R-matrix pole was tried but gave a much lower total cross section than the 1^{-} term. This assignment of $J^{\pi} = 1^{-}$ is consistent with all recent analyses (Lauritsen and Ajzenberg-Selove, 1966).

The cross sections predicted by the single pole, using the γ_c's given in Table I, provide the lines shown in Figures 9, 10 and 12 (at energies above about 50 KeV). It can be seen that the resonance shape does not perfectly fit the measurements in the energy range 150-280 KeV, with the theoretical cross sections rising to a value as much as 20% greater than the observed value. Alternatively, if this energy range had been fit well, the theoretical cross sections at low energies would have been much too low. Table I gives the interaction radii, the values of the γ_c's used in calculating the lines on Figures 7, 8, 9, 10 and 12, and the dimensionless reduced widths θ_c^2. The same interaction radii were used for all levels.

2). Direct Reactions. It was found that the direct reaction amplitudes were not qualitatively or quantatively important in explaining the observed cross sections and angular distributions. An upper limit of $Q \simeq 10$ (see Appendix G for a definition of Q) for the (p,d) reaction was estimated by calculating the amplitude of the

exponential tail of a neutron bound by 1.67 MeV in a square well of radius R_c . The direct interaction of this strength would produce a cross section of about 0.3 mbarn at 300 KeV, and an effect of only 1-5% in the $P_1(\cos\theta)$ term in $d\sigma/d\Omega$. The variation with energy of the direct reaction cross section is nearly the same as that of the observed total cross section below 300 KeV, so the direct reactions can cause no low energy enhancements in d_1/d_o resembling those in Figure 7. Because of the additional exponential in $I_{\ell\ell'}$, the (p,α) direct reaction amplitude is much smaller than the (p,d) amplitude. Thus the (p,α) direct reaction is negligible.

3). <u>-20 KeV Level.</u> This state in ^{10}B has been observed in $\alpha + {}^6Li$ and $^9Be(^3He,d)$ reactions, among others (Lauritsen and Ajzenberg-Selove, 1966). Forsyth, et al (1966), using the $^9Be(^3He,d)$ reaction, assigned a positive parity and $J = 1$, 2, or 3 to this state. Meyer, et al (1967), studying the $\alpha + {}^6Li$ elastic scattering, assigned a negative parity with $J = 2$ or 4.

In order to explain the large low energy asymmetries (Figures 7 and 8), it is necessary for the -20 KeV state to have opposite parity to the 310 KeV level (i.e., positive parity). The analysis of Meyer, et al (1967) in terms of an f-wave alpha particle resonance does not fit their observed excitation functions adequately at all angles. Their ignoring of the $d + {}^8Be$ channel by using a single channel theory is certainly incorrect if the deuteron reduced width has the magnitude suggested by the tentative value in Table I. This value was needed in our analysis to explain the deuteron asymmetry at low energy.

This level had the effect of increasing the very low energy cross sections by about 20% to 40%. The effect on σ was negligible above about 50 KeV. A reasonable choice of γ_c's could give an S function which actually increased at low energies, although the asymmetries would not be fitted as well. The presence of this level complicates the determination of thermonuclear reaction rates, which would normally be quite accurately predictable with experimental cross section data at energies below 50 KeV. Because it is uncertain whether the effect seen at the very low energy end of Figure 12 is real or not, the value of $S_{cm}(0)$ has the large uncertainties given in Section III, Part D.

In view of the importance of this level in determining the very low energy ^{9}Be(p,d) and (p,α) cross sections, and the uncertainty in its J^π, it would be worthwhile to study in more detail the ^{6}Li(α,α) and ^{6}Li(α,d) reactions at this resonance. A determination of the deuteron and alpha reduced widths for this level, when combined with the angular distribution data in this work might allow a reasonably accurate prediction of the S function at very low energies.

4). <u>410 KeV Level.</u> Because of the large asymmetry in the cross sections above 400 KeV, and the definite resonance shape seen in low angle production near 470 KeV (lab), the excited state at this energy is almost certainly of positive parity. The parameters used for this level did not fit the behavior of σ, the α asymmetry, or d_2/d_o for E > 400 KeV. The reactions above 400 KeV, however, are dominated by at least two broad levels of differing parities whose parameters would

be very difficult to determine from the experimental cross sections (see Figures 7, 8 and 9, and Thomas, et al, 1949). The parameters in Table I were chosen primarily to fit the asymmetries below 350 KeV, because the properties at higher energies are quite dependent on further levels.

A 1^+, 2^+ or 3^+ assignment is possible for this state, although 1^+ is slightly preferred. This is because the s-wave reduced width amplitudes for the deuteron and alpha channels had a greater effect than the d-wave widths when fitting the asymmetries at the lower energies.

To summarize, this analysis provided four important conclusions:

1) The qualitative and quantitative aspects of the cross sections below 300 KeV are completely explained by compound nucleus formation.
2) Qualitatively, the results for higher energies are also due to compound nucleus interactions.
3) The ^{10}B level at 6.56 MeV excitation energy probably has positive parity, with $J = 2$ or 3.
4) The level at 7.00 MeV has positive parity and $J = 1$, 2, or 3 with $J = 1$ favored.

APPENDIX

A. Kinematic Correction Factors

The conversion factors used for converting from the center-of-mass system to the lab system were (Evans, 1955; Marion and Young, 1968):

$$d\sigma_{cm}/d\sigma_{lab} = \cos(\theta_{cm} - \theta_{lab}) \sin^2\theta_{lab}/\sin^2\theta_{cm} \tag{A.1}$$

$$\sin(\theta_{cm} - \theta_{lab}) = f \sin \theta_{lab} \tag{A.2}$$

$$f = \left[\frac{m_1 m_3 (m_3 + m_4) E}{m_4 (m_1 + m_2)(Em_2 + Q(m_1+m_2))} \right]^{1/2} \tag{A.3}$$

$$Q = (m_1 + m_2 - m_3 - m_4) c^2 \tag{A.4}$$

Particle 1 is the proton, particle 2 is the ^{9}Be nucleus, particle 3 is the observed product and particle 4 is the recoil product nucleus. E is the lab energy of the proton. The same formulas are applied to the Rutherford scattering of alphas, with $m_1 = m_3$ and $m_2 = m_4$.

B. Rutherford Scattering Cross Section (Evans, 1955)

$$E^2 d\sigma/d\Omega = (Z_1 Z_2/4r)^2 \csc^4(\theta_{cm}/2) \tag{B.1}$$

$r = m_{Be}(m_{Be}+m_\alpha)^{-1}$, Z_1 = alpha charge = 2e , Z_2 = Be charge = 4e and θ_{cm} = center-of-mass scattering angle.

C. Solid Angle Corrections

The beam spot was observed (by discoloration of the target) to lie 1.4 mm to one side of the axis of the target chamber. This meant that the solid angle of the detectors varied as a function of angle.

The raw angular distribution data were corrected for the varying distances of the detectors from the beam spot.

Referring to Figure 13, we see that the distances of the detectors from the beam spot were:

$$\text{Detector 1 :} \quad r_1 = r_o - d \sin(\theta_1 + 45^o),$$

$$\text{Detector 2 :} \quad r_2 = r_o + d \sin(\theta_2 - 45^o),$$

where $d = 2.0 \pm .2$ mm .

The counting rates for detector number n were corrected by multiplying them by r_n^2/r_o^2 .

D. Effective Charge Correction

When bombarding the thin targets, the current collected at the Faraday cup was less than that measured with the target removed. This reduction was due to the charge state of the proton beam being changed in the target, and to scattering of a fraction of the incident beam out of the solid angle of the Faraday cup. The magnitude of this effect was measured by integrating a steady beam current to a certain charge value, with and without the target in position. The correction factor which was used to multiply the raw counting rates is shown in Figure 14.

E. Corrections to Incident Energy Due to Impurity Buildup

The very low energy cross section measurements required bombarding the target with up to .3 Coulombs of protons. During the period of the run, a significant thickness of carbon would build up on the surface of the target. This caused the energy of the particles reaching the beryllium to vary during a run. The magnitude of this effect was

estimated by measuring the counting rate at an initial energy of 145 KeV before and after each run. Knowing the excitation curve slope near 145 KeV and dE/dx values for carbon (Williamson, et al, 1966) allowed the calculation of the thickness deposited on the target during the run.

The average counting rate observed is:

$$\frac{1}{T}\int_0^T \text{rate}(t)\,dt \;\propto\; (1/\Delta E)\int_{E_o}^{E_o-\Delta E} S(E)\,\exp(-b/E^{1/2})\,dE/E \quad . \qquad (E.1)$$

T = duration of the run, $E = E_o - \Delta E\ t/T$, E_o = initial beam energy, $E_o - \Delta E$ = final beam energy, and b is defined in Section III.D. Since ΔE was never larger than 5 KeV, this integral was approximated by:

$$\int_{y_i}^{y_f} f(y)\,dy = \frac{y_f - y_i}{4}\left(f(y_f) + f(y_i) + 2f\left(\frac{y_f + y_i}{2}\right)\right) \qquad (E.2)$$

resulting in a counting rate proportional to:

$$\sigma(\bar{E})\left(1 + \cosh\left(\frac{y_f - y_i}{2}\right)\right) / 2 \qquad (E.3)$$

where $\bar{E} = E_o - \Delta E/2$, $y_f = b/(E_o - \Delta E)^{1/2}$, and $y_i = b/E_o^{1/2}$.

Thus, the average counting rate observed was the same as would be observed with a beam energy of $E_o - \Delta E/2$, with no target buildup, with the correction included. The correction was less than 1.1 for energies above 40 KeV. The points on the excitation curves (Figures 9 and 10) are placed at $E_o - \Delta E/2$.

F. Target Thickness Corrections

Because of the energy lost in the target by the incoming protons, the measured counting rate was less than would be measured if the beam

had had its initial energy throughout the target. The counting rate was proportional to:

$$\int_0^d \sigma(E)dx = (dE/dx)^{-1} \int_{E_i}^{E_f} S(E)\ \exp(-b/E^{1/2})\ dE/E \quad , \qquad (F.1)$$

where d is the Be target thickness, and $E = E_i + xdE/dx$. Using the same approximation as in Part E, the counting rate is proportional to:

$$\sigma(E_i)\ d[1 + 2E_i S(\bar{E})\ \exp(\frac{y_i - y_f}{2}) / \bar{E}S(E_i)$$

$$+ E_i S(E_f)\ \exp(y_i - y_f) / E_f S(E_i)] / 4 \qquad (F.2)$$

$$E_f = E_i + d\ dE/dx \quad \text{and} \quad \bar{E} = (E_i - E_f) / 2 \quad .$$

This approximation is reasonable for energies above about 30 KeV, for a 10 $\mu g/cm^2$ target.

The inverse of the quantity multiplying $d\sigma(E_i)$ in equation F.2 is multiplied by the observed counting rate to give a rate proportional to the true cross section at $E = E_i$. This correction factor is plotted in Figure 15 for a target thickness of 22 $\mu g/cm^2$, and in Figure 16 for a target thickness of 10 $\mu g/cm^2$.

G. Theoretical Cross Section Formulas

In the formulas of this section, primed quantities refer to final state channels, while unprimed quantities refer to initial state channels. Symbols that are not mentioned in the text are defined in Appendix H.

Cross Sections

For unpolarized initial and final states,

$$d\sigma/d\Omega' = \frac{\sum_{s,s'} (2s+1)\ (d\sigma/d\Omega')_{ss'}}{\sum_{s} (2s+1)} \quad , \tag{G.1}$$

$$(d\sigma/d\Omega')_{ss'} = (k^2(2s+1))^{-1} \sum_{L} B_L(s,s')\ P_L(\cos\theta') \quad , \tag{G.2}$$

$$B_L(s,s') = \frac{(-)^{s-s'}}{4} \sum_{\substack{\ell_1,\ell_1',J_1 \\ \ell_2,\ell_2',J_2}} \overline{Z}(\ell_1,J_1,\ell_2,J_2;s,L)\overline{Z}(\ell_1',J_1,\ell_2',J_2;s',L) \times (T^{J_1^\pi}_{\alpha_1'\alpha_1})(T^{J_2^\pi}_{\alpha_2'\alpha_2})^* \quad , \tag{G.3}$$

$$\overline{Z} = ((2\ell_1+1)(2\ell_2+1)(2J_1+1)(2J_2+1))^{1/2} \begin{pmatrix} \ell_1 & \ell_2 & L \\ 0 & 0 & 0 \end{pmatrix} \begin{Bmatrix} \ell_1 & J_1 & s \\ J_2 & \ell_2 & L \end{Bmatrix} \tag{G.4}$$

and

$$T^{J^\pi} = T^{\text{direct}} + T^{\text{comp.nuc.}} \quad . \tag{G.5}$$

Direct Reactions

$$T^{\text{direct}} = (i/\hbar) \int \phi_p^*\ V^{\text{ext}}\ \psi_{\text{out}}\ dx \tag{G.6}$$

$$\phi_p = 2N_1 \exp(-i\omega_\ell)(i)^{\ell+2}(F_{\ell\eta}(k_p r_p)\ \phi_8(r_{\alpha_1} - r_{\alpha_2})\exp(-\beta_1 r_n)/(r_p v_p^{1/2})) \times \sum_{\text{all } m's} \begin{pmatrix} \ell & s & J \\ m_2 & m_1 & M \end{pmatrix} \begin{pmatrix} 1 & \frac{1}{2} & s_N \\ m & m_n & m_N \end{pmatrix} \begin{pmatrix} s_N & \frac{1}{2} & s \\ m_N & m_p & m_1 \end{pmatrix} U^{m_p}_{1/2}\ U^{m_n}_{1/2}\ Y^{m_2}_{\ell}(\Omega_p) Y^{m}_{1}(\Omega_n) \tag{G.7}$$

For the $^{8}Be + d$ exit channel,

$$\phi_{out} = -2(i)^{\ell'+1} \exp(i\omega'_{\ell'})(F_{\ell'\eta'}(k_d r_d)\phi_d(r_{np})\phi_8(r_{\alpha_1}-r_{\alpha_2})/(r_d v_d^{1/2}))$$
$$\times \sum_{m's} \begin{pmatrix} \ell' & s' & J \\ m'_2 & m'_1 & M \end{pmatrix} \begin{pmatrix} \frac{1}{2} & \frac{1}{2} & s' \\ m_p & m_n & m'_1 \end{pmatrix} U^{m_p}_{1/2} U^{m_n}_{1/2} Y^{m'_2}_{\ell'}(\Omega_d) \quad . \tag{G.8}$$

For the $^{6}Li + \alpha$ channel,

$$\phi_{out} = -2N_2(i)^{\ell'+1} \exp(i\omega'_{\ell'})(F_{\ell'\eta'}(k_\alpha r_{\alpha_2})\phi_d(r_{np})\phi_L(r_{\alpha_1}-r_d)/(r_{\alpha_2} v_\alpha^{\frac{1}{2}}))$$
$$\times \sum_{m's} \begin{pmatrix} \ell' & s' & J \\ m'_2 & m'_1 & M \end{pmatrix} \begin{pmatrix} \frac{1}{2} & \frac{1}{2} & s' \\ m_p & m_n & m'_1 \end{pmatrix} U^{m_p}_{1/2} U^{m_n}_{1/2} Y^{m'_2}_{\ell'}(\Omega_{\alpha_2}) \quad . \tag{G.9}$$

The interaction V^{ext} is defined by:

$$\phi_d(r_{np})\, V^{ext}(r_{np}) = A_1 \delta^3(r_{np}) \quad . \tag{G.10}$$

Choosing this form for V^{ext} and $\phi_L(r_{\alpha_1} - r_d) = \delta^3(r_{\alpha_1} - r_d)$ causes all the solid angle arguments of the spherical harmonics in G.7 to G.9 to be identical. Thus, the angular integration in the integral for T^{direct} reduces to an integral of a product of three spherical harmonics of the same argument:

$$\int Y^{*m_2}_{\ell} Y^{*m}_{1} Y^{m'_2}_{\ell'} \, d\Omega = (3(2\ell+1)/(4\pi(2\ell'+1)))^{1/2} \begin{pmatrix} \ell & 1 & \ell' \\ m_2 & m & m'_2 \end{pmatrix} \begin{pmatrix} \ell & 1 & \ell' \\ 0 & 0 & 0 \end{pmatrix} \tag{G.11}$$

The summation over magnetic quantum numbers of the six Clebsch-Gordan coefficients occurring in T^{direct} results in a product of two 6-j coefficients, multiplied by some numbers and a phase. Finally,

$$T^{direct} = i(Q/k)(AA'/(kk'))^{1/2}\ (-)^{P}\ \exp(i(\omega_{\ell}+\omega'_{\ell'}))\ K$$

$$\times \begin{pmatrix} \ell & 1 & \ell' \\ 0 & 0 & 0 \end{pmatrix} \begin{Bmatrix} 1 & \frac{1}{2} & \frac{3}{2} \\ \frac{1}{2} & s & 1 \end{Bmatrix} \begin{Bmatrix} 1 & 1 & s \\ J & \ell & \ell' \end{Bmatrix}\ R\ I_{\ell\ell'} \quad , \tag{G.12}$$

$$I_{\ell\ell'} = \int_{a}^{\infty} F_{\ell\eta}(r)\ F_{\ell'\eta'}(\gamma r)\ \exp(-\beta r)\ dr \quad , \tag{G.13}$$

$$P = \frac{\ell + \ell' - 1}{2} + s + J$$

and

$$K = ((2\ell+1)(2s+1))^{1/2}\ \frac{2J+1}{2\ell'+1} \quad .$$

For the $d + {}^{8}Be$ exit channel,

$$Q = 12A_1N_1m_p/(\hbar^2\pi^{1/2}) \ , \qquad R = (1+m_p/m_9)\ /\ (1+m_d/m_8) \ ,$$

$$\gamma = k/(k'R) \quad , \quad \text{and} \qquad \beta = \beta_1\gamma/k \quad . \tag{G.14}$$

For the $\alpha + {}^{6}Li$ channel,

$$Q = 12A_1N_1N_2m_p\ /\ (\hbar^2\pi^{1/2}) \ , \ R = (1+m_p/m_9)\ /\ (1+m_d/m_L+m_d/m_\alpha+m_\alpha/m_L),$$

$$\gamma = k/(k'R) \quad , \quad \text{and} \qquad \beta = (\beta_1+\beta_2)\gamma/k \quad . \tag{G.15}$$

The lower limit a of the integral $I_{\ell\ell'}$ is k times the interaction radius. This limit was changed to zero to make an analytic solution possible. The integral was calculated numerically for the true lower limit and found to be only 0-5% too small, with the error increasing with energy. This approximation overestimates $I_{\ell\ell'}$. An analytic representation for $I_{\ell\ell'}$ (with $a = 0$) in terms of

hypergeometric functions was found. Because of the Clebsch-Gordan "parity" coefficient in the expression for T^{direct} (Eq. G.12), only values of $I_{\ell\ell'}$ for $\ell' = \ell \pm 1$ are needed. For $\ell' = \ell + 1$,

$$I_{\ell\ell'} = \sum_{n=1}^{3} A_{\ell_n} J_{\ell_n} \quad , \tag{G.16}$$

while with $\ell' = \ell - 1$,

$$I_{\ell\ell'} = \sum_{n=1}^{3} B_{\ell_n} J_{\ell_n} \quad . \tag{G.17}$$

$$B^*_{\ell 3} = B_{\ell 1} = (\ell(\ell+1) - \eta'^2 - i\eta'(2\ell+1)) \,/\, (2\ell(2\ell+1)) \ ,$$

and $$B_{\ell 2} = (\ell^2+\eta'^2) \,/\, (\ell(2\ell+1)) \quad . \tag{G.18}$$

$$-A_{\ell 2}/2 = A_{\ell 1} = A_{\ell 3} = -(2\ell+2)(2\ell+3) \,/\, (4\gamma^2) \quad . \tag{G.19}$$

$$J_{\ell n} = (2\ell+1)! \ {}_2F_1(\ell+n-1 + i\eta', \ \ell+1 - i\eta \ ; \ 2\ell+2 \ ; \ 4\gamma/q^2)$$

$$\times \ (r^{n-2}/q^{2\ell+n}) \ \exp(S+iQ) \ , \tag{G.20}$$

where

$$S = \eta'(\theta+\phi) + \eta(\theta-\phi) \quad , \quad Q = (\eta-\eta')\log_e(q/r) + (2-n)(\theta+\phi) \ ,$$

$$\theta = \tan^{-1}((\gamma+1) \,/\, \beta) \quad , \quad \phi = \tan^{-1}((\gamma-1)/\beta) \ ,$$

$$r^2 = \beta^2 + (\gamma-1)^2 \quad , \text{ and } \quad q^2 = \beta^2 + (\gamma+1)^2 \ . \tag{G.21}$$

Compound Nucleus

$$T^{\text{compound nucleus}} = C^{-1} \, D \tag{G.22}$$

$$C = (I - RL_o) \, \Omega^{-1} \, W \tag{G.23}$$

$$D = -(I - RL_o^*)\Omega \quad W \tag{G.24}$$

I, L_o, Ω and W are diagonal matrices:

$$I_c = 1 \quad , \qquad W_c = (P_c)^{-1/2} \quad , \quad \Omega_c = \exp(i(\omega_c - \phi_c)) \quad ,$$

$$(L_o)_c = S_c - B_c + iP_c \quad , \quad \omega_c = \sum_{n=1}^{\ell} \tan^{-1}(\eta_c/n) \quad , \quad \phi_c = \tan^{-1}(F_c/G_c),$$

$$P_c = \frac{\rho_c}{F_c^2 + G_c^2} \qquad \text{and} \qquad S_c = P_c(F_c F_c' + G_c G_c') \quad . \tag{G.25}$$

B_c is the logarithmic derivative boundary condition on the wave function at the interaction radius. B_c was taken equal to the value of S_c at the energy of the R-matrix pole. F_c and G_c are the regular and irregular Coulomb wave functions for the channel c evaluated at $\rho_c = k_c R_c$.

R is a real matrix:

$$R_{cc'}^{J^\pi} = \gamma_c \gamma_c' / (E_p - E) \quad , \tag{G.26}$$

where the γ_c's are the reduced width amplitudes for the various channels c , and E_p is the location of the energy pole in the R-matrix.

The parameters varied in fitting the experimental data were the three channel interaction radii R_c , and the values of E_p and the γ_c's for each pole.

H. Glossary of Symbols Used in Appendix G

Symbol	Definition
a	lower limit of the $I_{\ell\ell'}$ integral; $a=kR_p$
c,c'	channel labels; determined by ℓ, s and the type of particles in the channel
k,k',k_p,etc.	wave numbers; $k_i = (2M_iE_i)^{1/2}/\hbar$
ℓ,ℓ_1,ℓ_2,etc.	orbital angular momentum values
m,m_n,m_2,etc.	orbital angular momentum space projections
n	summing index
r,r_n,r_p,etc.	radial coordinates; r_i is the distance of particle i from the center-of-mass
r_{np}	separation of the neutron from the proton
s,s'	channel spins
s_N	spin of the ^{9}Be nucleus; s_N= 3/2
v_p,v_n,etc.	channel velocities; $v_i = \hbar k_i/M_i$
A,A'	ratio of the channel reduced mass to the proton rest mass
A_1	strength of the n-p zero-range interaction
E,E_p,etc.	particle energy in the center of mass
$F_{\ell\eta}$	regular Coulomb wave function
$G_{\ell\eta}$	irregular Coulomb wave function
J	total angular momentum of a state
L	index of Legendre polynomial term in $d\sigma/d\Omega$
M,M_p,etc.	rest mass of a particle or channel reduced mass
N_1,N_2	amplitude of the exponential "tails" in the neutron and alpha wave functions in ^{9}Be

Symbol	Definition
P_L	Legendre polynomial
R_c	channel interaction radius
$T^{J\pi}$	transition matrix for states of a given total angular momentum and parity
T^{direct}	transition matrix for direct reaction processes
$T^{comp.nuc.}$	transition matrix for compound nucleus reactions
$U^m_{1/2}$	spin 1/2 wave function for proton and neutron
V^{ext}	interaction between proton and bound neutron in the region outside the compound nucleus interaction radius
Y^m_ℓ	spherical harmonic angular wave function
α_1, α_1', etc.	channel labeling indices; α_1 is shorthand for ℓ_1, s
β_1, β_2	inverse decay lengths for the neutron and alpha particle in the ^{9}Be nucleus
η, η'	Coulomb parameter; $\eta_c = Z_1 Z_2 e^2/(\hbar v_c)$
σ	cross section
$d\sigma/d\Omega'$	differential cross section; subscripts ss' refer to the differential cross section for an incoming state of spin s to be scattered into a final state of spin s'
ϕ_d	deuteron radial wave function
ϕ_L	radial wave function of the deuteron and alpha particle in a simplified model of ^{6}Li
ϕ_8	radial wave function of the alphas in the core of the ^{9}Be nucleus
ω_ℓ	Coulomb phase; $\omega_\ell = \sum_{s=1}^{\ell} \tan^{-1}(\eta/s)$
Ω_i	solid angle for coordinates i
θ_c^2	ratio of γ_c^2 to the Wigner limit; $\theta_c^2 = \gamma_c^2 \frac{2M_c R_c^2}{3\hbar^2}$

Symbol	Definition
$\begin{pmatrix} \ell_1 & \ell_2 & \ell_3 \\ m_1 & m_2 & m_3 \end{pmatrix}$	Clebsch-Gordan vector addition coefficient
$\begin{Bmatrix} j_1 & j_2 & j_3 \\ J_1 & J_2 & J_3 \end{Bmatrix}$	Wigner 6-j coefficient

REFERENCES

Abramowitz, M. and Stegun, I.E., 1964, Handbook of Mathematical Functions, National Bureau of Standards AMS-55, U.S. Government Printing Office

Armstrong, J.C., Mullendore, J.V., Harris, W.R. and Marion, J.B., 1965, Proc. Phys. Soc. (London 86, 1283

Audouze, J., 1970, Astron. and Astrophys. 8, 436

Davids, C.N., 1968, Nucl. Phys. A110, 619

Elwyn, A.J., Monahan, J.E. and Schiffer, J.P., 1971, Nuclear Fusion 11, 551

Evans, R.D., 1955, The Atomic Nucleus, McGraw-Hill Book Company, Inc., New York

Forsyth, P.D., Knudson, A.R. and Young, F.C., 1966, Nucl. Phys. 85, 153

Fowler, W.A., Caughlan, G.R. and Zimmerman, B.A., 1967, Ann. Rev. of Astron. and Astrophys. 5, 525

Gradshteyn, I.S. and Ryzhik, I.M., 1965, Table of Integrals; Series, and Products, Academic Press, Inc., New York

Lane, A.M. and Thomas, R.G., 1958, Rev. Mod. Phys. 30, 257

Lauritsen, T. and Ajzenberg-Selove, F., 1966, Nucl. Phys. 78, 1

McNally, J.R. Jr., 1971, Nuclear Fusion 11, 187, 554

Marion, J.B. and Young, F.C., 1968, Nuclear Reaction Analysis, American Elsevier Publishing Company, Inc., New York

Meyer, V., Pixley, R.E. and Truöl, P., 1967, Nucl. Phys. A101, 321

Mozer, F.S., 1956, Phys. Rev. 104, 1386

Neuendorffer, J.A., Inglis, D.R. and Hanna, S.S., 1951, Phys. Rev. 82, 75

Reeves, H., 1971, Nuclear Reactions in Stellar Surfaces and Their Relations with Stellar Evolution, Gordon and Breach Science Publishers, New York

Reeves, H. and Audouze, J., 1968, Astrophys. Lett. 1, 197

Robinson, D.C., 1967, Nucl. Phys. A95, 663

Thomas, R.G., 1955, Phys. Rev. 100, 25

Thomas, R.G., Rubin, S., Fowler, W.A. and Lauritsen, C.C., 1949, Phys. Rev. 75, 1612

Wagoner, R.V., 1969, Ap. J. Suppl. 18, #162, 247

Wallerstein, G. and Conti, P.S., 1969, Ann. Rev. of Astron. and Astrophys. 7, 99

Weber, G., Davis, L.W. and Marion, J.B., 1956, Phys. Rev. 104, 1307

Williamson, C.F., Boujot, J.P. and Picard, J., 1966, Report CEA-R 3042, Center for Nuclear Studies, Saclay

TABLE I

The parameters of the three R-matrix poles used in fitting the experimental cross sections. The first two columns give the energy (in MeV) and J^{π} values of the levels. The next two give the channel identification and the interaction radii in fm. The final columns give the ℓ and s values, the reduced width amplitudes used (in MeV), and $\theta_c^2 = \gamma_c^2(2M_cR_c^2/3\hbar^2)$. These R-matrix parameters are discussed on pages 18 to 24 .

E_{cm}	J^{π}	Channel	R_c	ℓ	s	γ_c	θ_c^2
		p		0	1	.65	.34
		p	7.4	2	1	.50	
.310	1^-	p		2	2	.51	
		d	8.0	1	1	.28	.15
		α	8.6	1	1	.15	.055
		p		1	1	.10	.01
		p		3	1	.10	
-.020	2^+	p	7.4	1	2	.11	
		p		3	2	.11	
		d	8.0	2	1	.50	.6
		α	8.6	2	1	-.05	.006
		p		1	1	.60	.3
		p	7.4	1	1	-.61	
		p		3	2	.20	
.410	1^+	d		0	1	.40	.3
		d	8.0	2	1	1.00	
		α	8.6	0	1	.20	.1
		α		2	1	.01	

TABLE II

The excitation functions for $^{9}Be(p,\alpha)$ and (p,d) . The table entries are: the proton lab energy in KeV, the (p,α) total cross section in millibarns, the (p,d) cross section and S_{cm} in MeV-barn as defined on page 9.

E_{lab}	σ_α	σ_d	S_{cm}
28	$(.55 \pm .3) \times 10^{-4}$	$(1.1 \pm .6) \times 10^{-4}$	75^{+15}_{-40}
36	$(5.5 \pm 1.5) \times 10^{-4}$	$(7.0 \pm 2.) \times 10^{-4}$	43^{+8}_{-14}
45	$(3.1 \pm .5) \times 10^{-3}$	$(2.9 \pm .5) \times 10^{-3}$	33^{+5}_{-8}
52	$(6.6 \pm .7) \times 10^{-3}$	$(7.2 \pm .7) \times 10^{-3}$	25 ± 5
58	$.022 \pm .002$	$.020 \pm .002$	28 ± 5
72	$.10 \pm .01$	$.09 \pm .01$	34 ± 4
82	$.32 \pm .03$	$.30 \pm .03$	47 ± 4
94	$.70 \pm .05$	$.72 \pm .05$	55 ± 5
105	$1.4 \pm .1$	$1.4 \pm .1$	58 ± 5
118	$2.6 \pm .2$	$2.6 \pm .2$	57 ± 5
130	$4.6 \pm .3$	$4.6 \pm .3$	61 ± 5
144	$7.5 \pm .5$	$7.5 \pm .5$	68 ± 5
160	$12.4 \pm .8$	$12.3 \pm .8$	84 ± 6
175	18.9 ± 1.0	19.2 ± 1.0	88 ± 6
192	29.5 ± 1.5	30.5 ± 1.5	95 ± 6
210	44 ± 2	45 ± 2	108 ± 7
227	69 ± 4	72 ± 4	132 ± 8
244	107 ± 6	113 ± 7	150 ± 9
262	162 ± 10	190 ± 12	183 ± 10
281	235 ± 16	268 ± 20	220 ± 12
300	295 ± 18	375 ± 26	260 ± 14
320	335 ± 20	435 ± 30	253 ± 14
341	350 ± 20	440 ± 30	232 ± 13

E_{lab}	σ_α	σ_d	S_{cm}
372	310 ± 17	400 ± 27	160 ± 10
405	275 ± 15	330 ± 25	115 ± 8
442	280 ± 15	320 ± 24	94 ± 7
468	290 ± 15	320 ± 22	86 ± 5
496	270 ± 14	310 ± 22	72 ± 5
522	250 ± 14	295 ± 21	64 ± 4
561	245 ± 14	275 ± 20	52 ± 4
603	245 ± 14	270 ± 20	47 ± 4
642	245 ± 14	265 ± 20	42 ± 3
697	260 ± 14	245 ± 20	37 ± 3

FIGURE 1

Angular distributions of deuterons from the $^{9}Be(p,d)^{8}Be$ reaction, normalized to the value at $\theta_{cm} = 90^{o}$, for proton lab energies of 115, 140, 175, 210 and 245 KeV. See page 6.

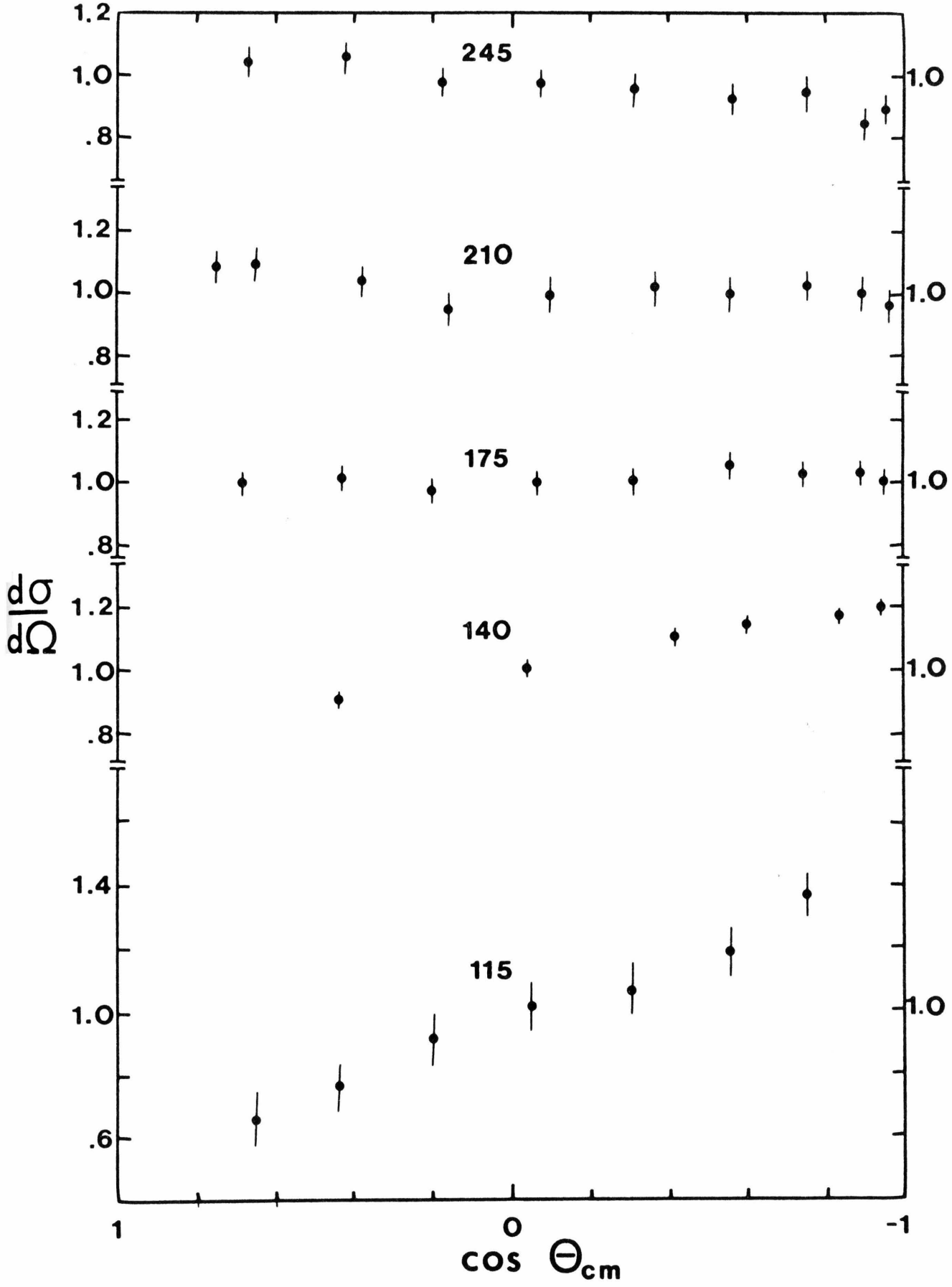
245
210
175
140
115
1.2
1.0
.8
1.4
.6
dσ/dΩ
1
0
-1
cos Θcm

FIGURE 2

Angular distributions of deuterons from the $^{9}Be(p,d)^{8}Be$ reaction, normalized to the value at $\theta_{cm} = 90^{o}$, for proton lab energies of 285, 325, 355 and 425 KeV. See page 6.

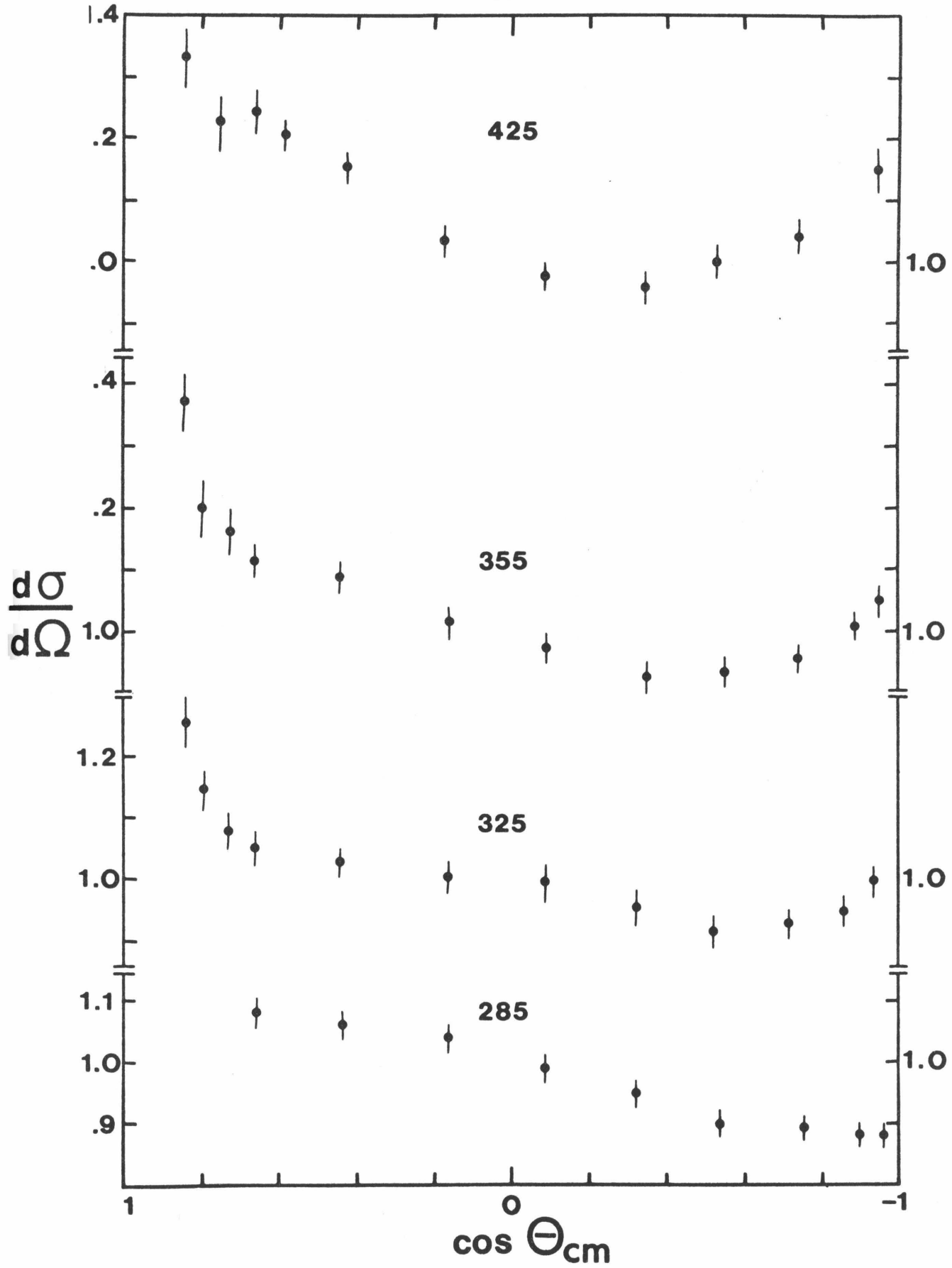
1.4
.2
.0
.4
.2
1.0
1.2
1.0
1.1
1.0
.9
425
355
325
285
1.0
1.0
1.0
1.0
dσ/dΩ
1
0
-1
cos Θcm

FIGURE 3

Angular distributions of deuterons from the $^{9}Be(p,d)^{8}Be$ reaction, normalized to the value at $\theta_{cm} = 90^{o}$, for proton lab energies of 480, 505, 550 and 600 KeV. See page 6.

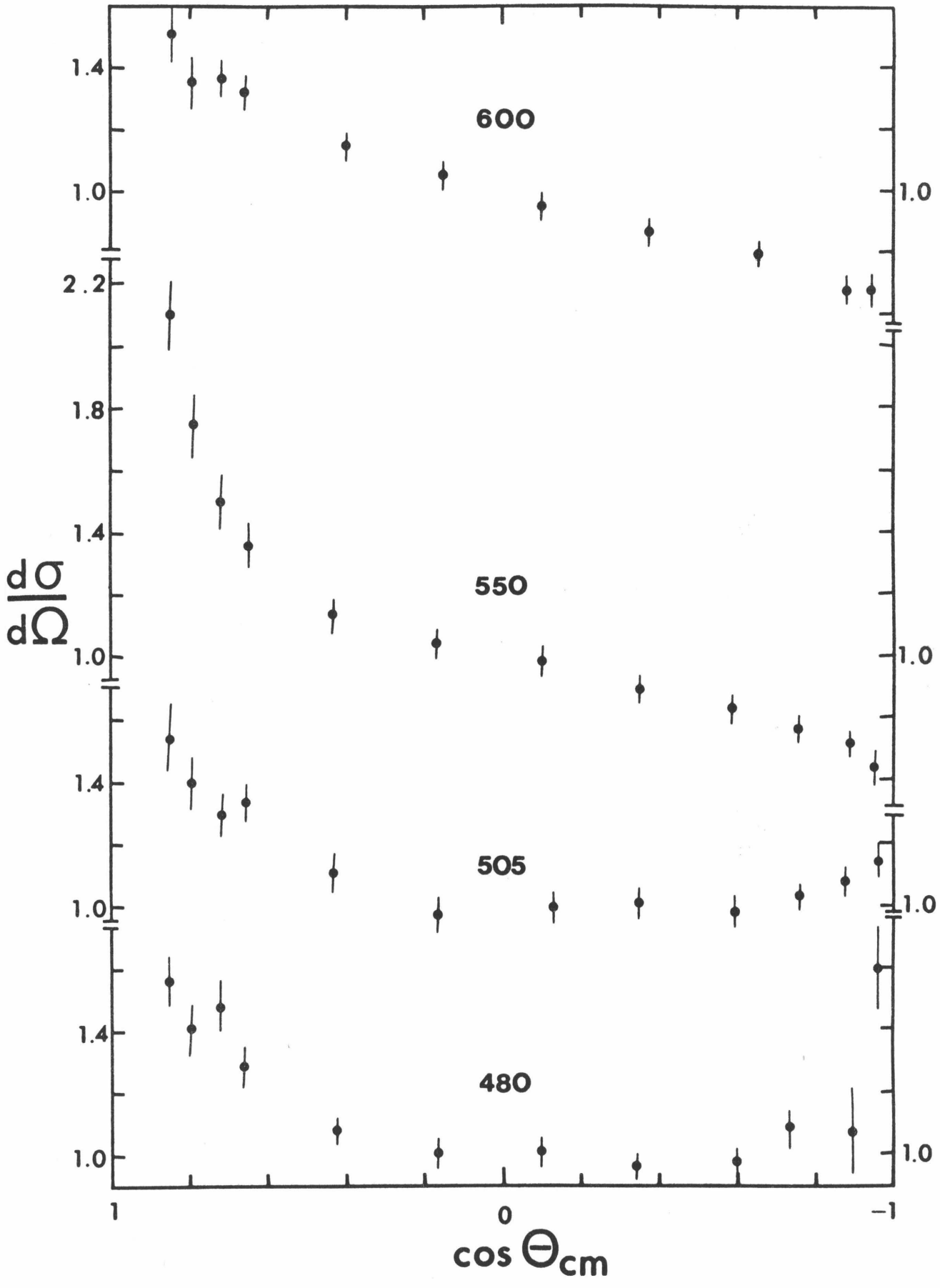
600
550
505
480
1.4
1.0
2.2
1.8
1.4
1.0
1.4
1.0
1.4
1.0
1.0
1.0
1.0
1.0
1
0
−1
cos Θcm
dσ/dΩ

FIGURE 4

Angular distributions of alphas from the $^{9}Be(p,\alpha)^{6}Li$ reaction, normalized to the value at $\theta_{cm} = 90^{o}$, for proton lab energies of 110, 145, 175, 210 and 245 KeV. See page 6.

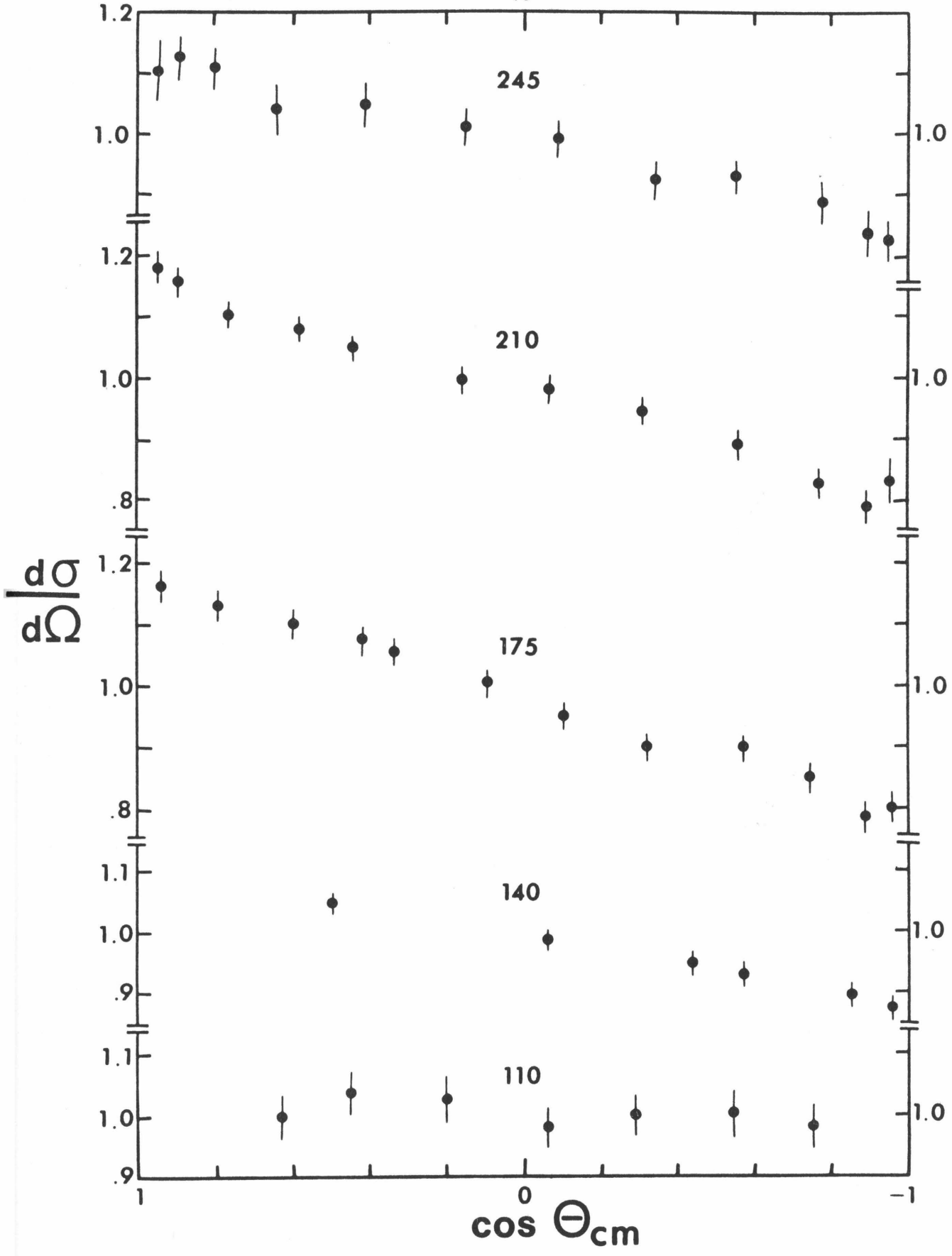
245
210
175
140
110
dσ/dΩ
cos Θcm
1
0
-1

FIGURE 5

Angular distributions of alphas from the $^{9}Be(p,\alpha)^{6}Li$ reaction, normalized to the value at $\theta_{cm} = 90^{o}$, for proton lab energies of 285, 325, 355, 390 and 425 KeV. See page 6.

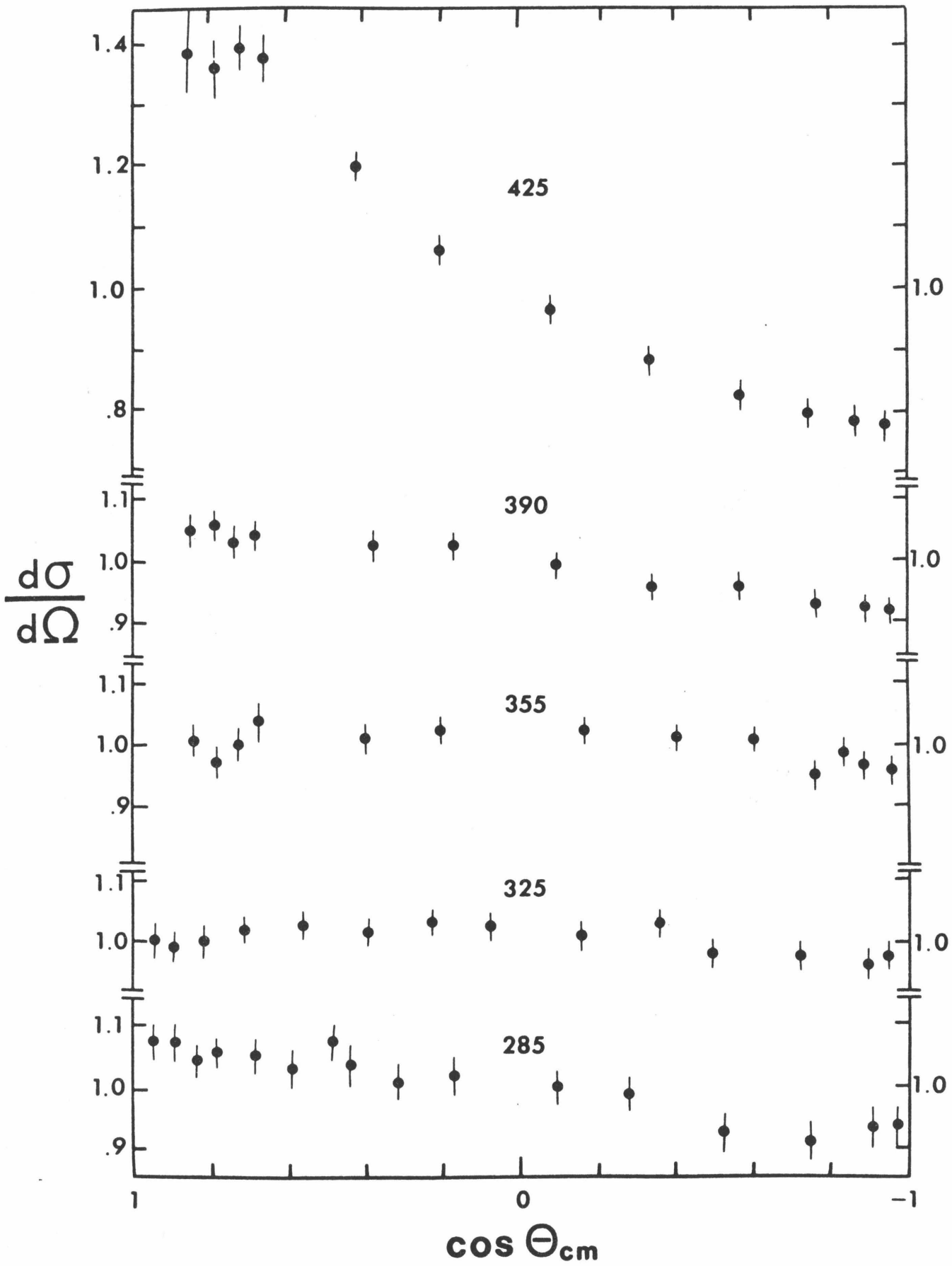
1.4
1.2
425
1.0
.8
1.1
390
1.0
.9
1.1
355
1.0
.9
1.1
325
1.0
1.1
285
1.0
.9
1.0
1.0
1.0
1.0
dσ/dΩ
1
0
−1
cos Θcm

FIGURE 6

Angular distributions of alphas from the $^{9}Be(p,\alpha)^{6}Li$ reaction, normalized to the value at $\theta_{cm} = 90^{o}$, for proton lab energies of 480, 505, 550 and 600 KeV. See page 6.

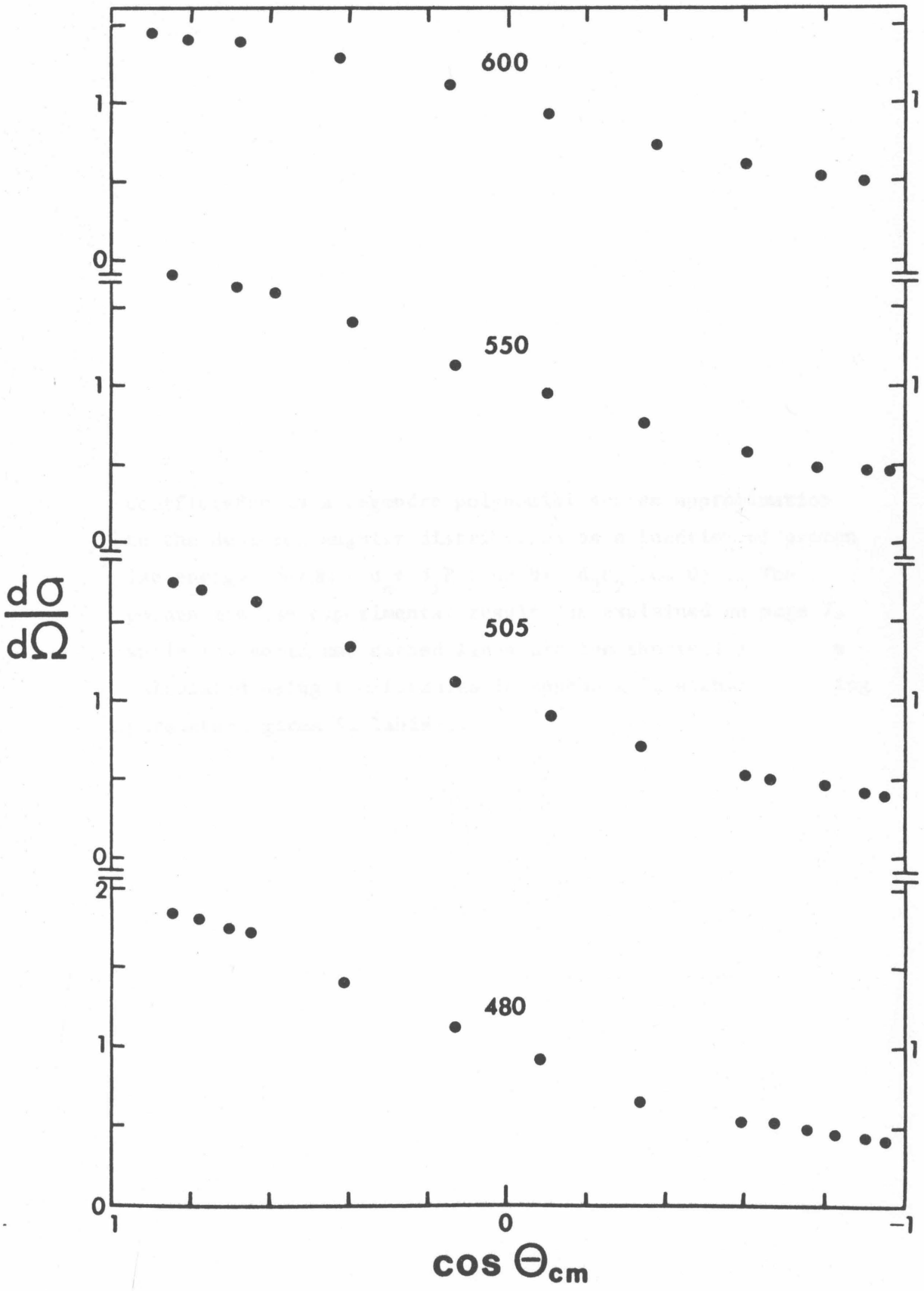
600
550
505
480
dσ/dΩ
cos Θcm
1
0
-1

FIGURE 7

Coefficients in a Legendre polynomial series approximation to the deuteron angular distribution as a function of proton lab energy $d\sigma/d\Omega = d_o + d_1 P_1(\cos\theta) + d_2 P_2(\cos\theta)$. The points are the experimental results as explained on page 7, while the solid and dashed lines are the theoretical values calculated using the formulas in Appendix G, with the fitting parameters given in Table 1.

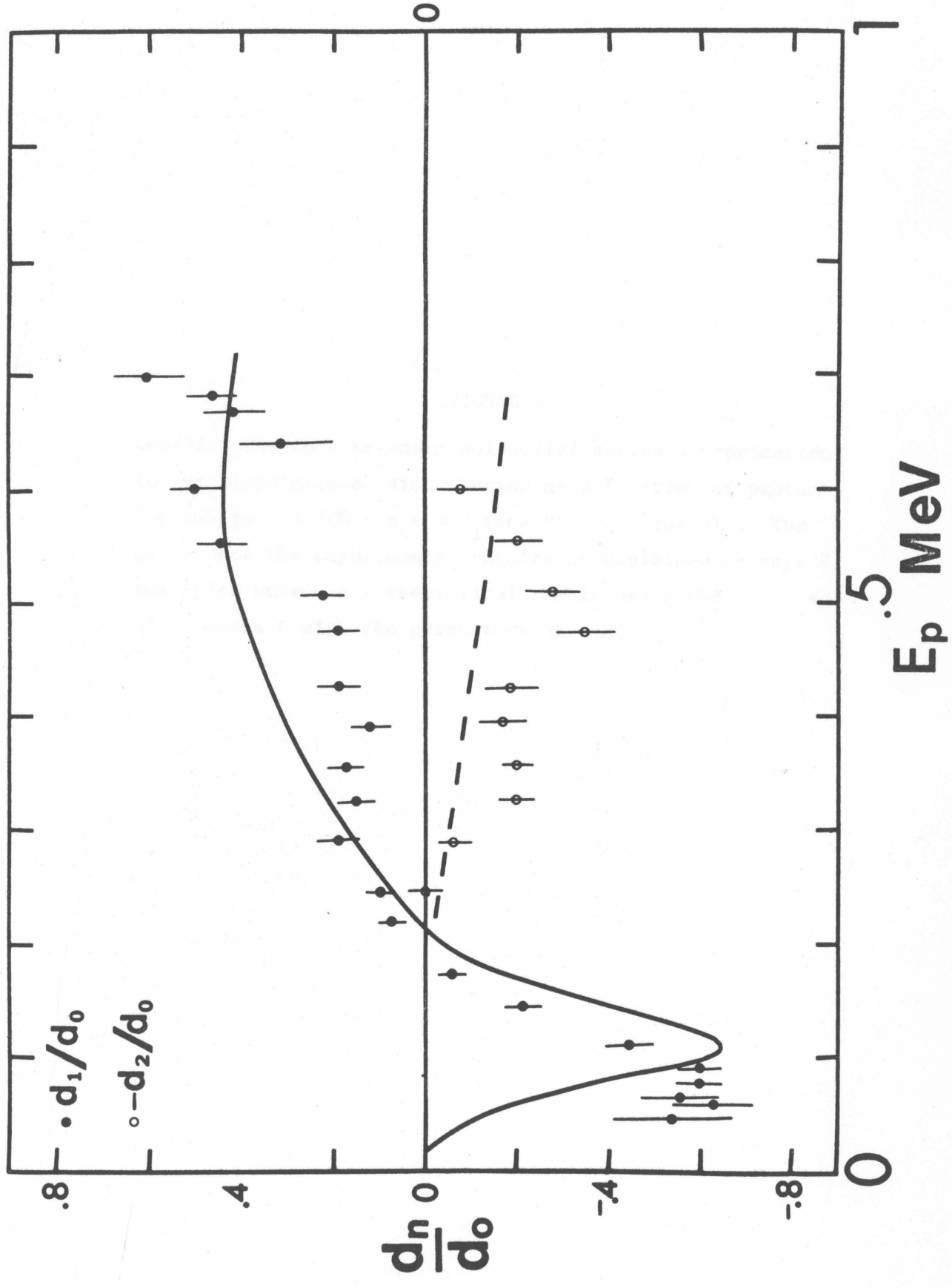
0
1
.5
E_p MeV
.8
.4
0
-.4
-.8
d_n/d_o
• d_1/d_o
◦ $-d_2/d_o$

FIGURE 8

Coefficients in a Legendre polynomial series approximation to the alpha angular distribution as a function of proton lab energy. $d\sigma/d\Omega = \alpha_o + \alpha_1 P_1(\cos\theta) + \alpha_2 P_2(\cos\theta)$. The points are the experimental results as explained on page 7, while the curve is a theoretical result using the formulas of Appendix G with the parameters of Table 1.

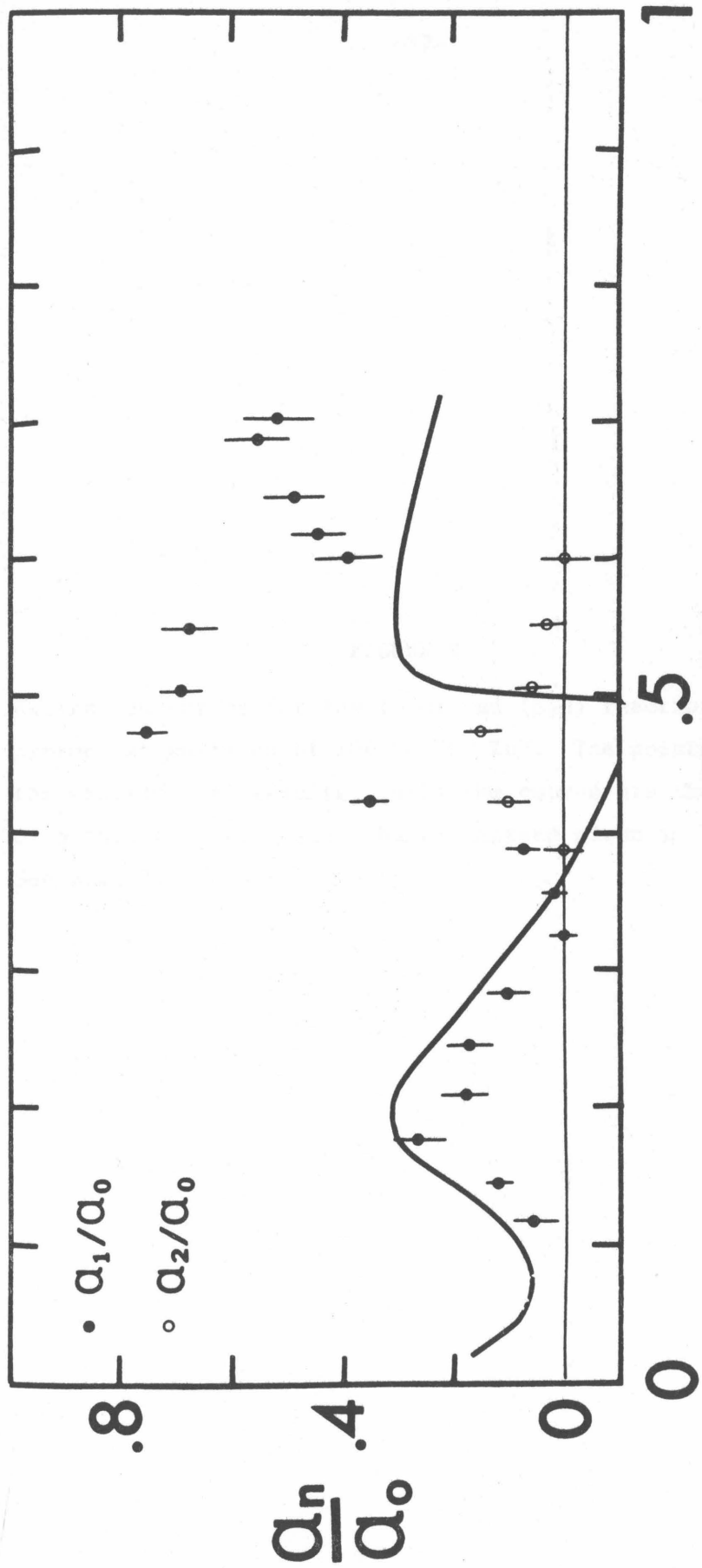
$\frac{a_n}{a_0}$
.8
.4
0
0
.5
1
E_p MeV
• a_1/a_0
∘ a_2/a_0

FIGURE 9

Excitation curves for the (p,α) and (p,d) reactions for proton lab energies of 100 to 700 KeV. The points are the experimental results, while the curves are the result of a theoretic fit using the parameters given in Table 1. See page 7.

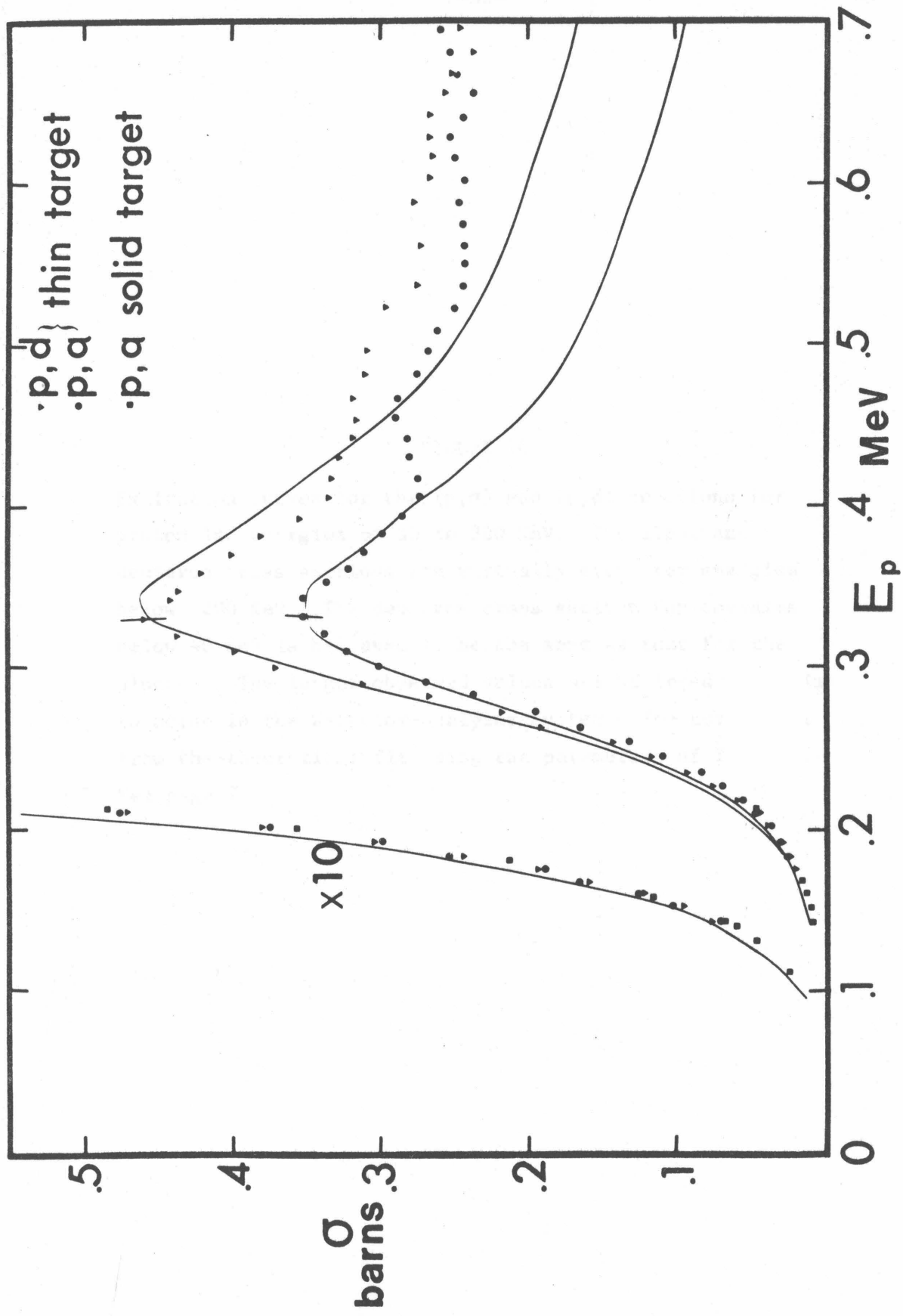
·p,d
·p,q } thin target
·p,q solid target
x10
σ
barns
.5
.4
.3
.2
.1
0
.1
.2
.3
.4
.5
.6
.7
E_p MeV

FIGURE 10

Excitation curves for the (p,α) and (p,d) reactions for proton lab energies of 30 to 300 KeV. The alpha and deuteron cross sections are virtually equal for energies below 200 KeV. The deuteron cross section for energies below 40 KeV is believed to be the same as that for the alphas. The larger observed values are believed to be due to noise in the detector-analyzer system. The curves are from the theoretical fit using the parameters of Table 1. See page 7.

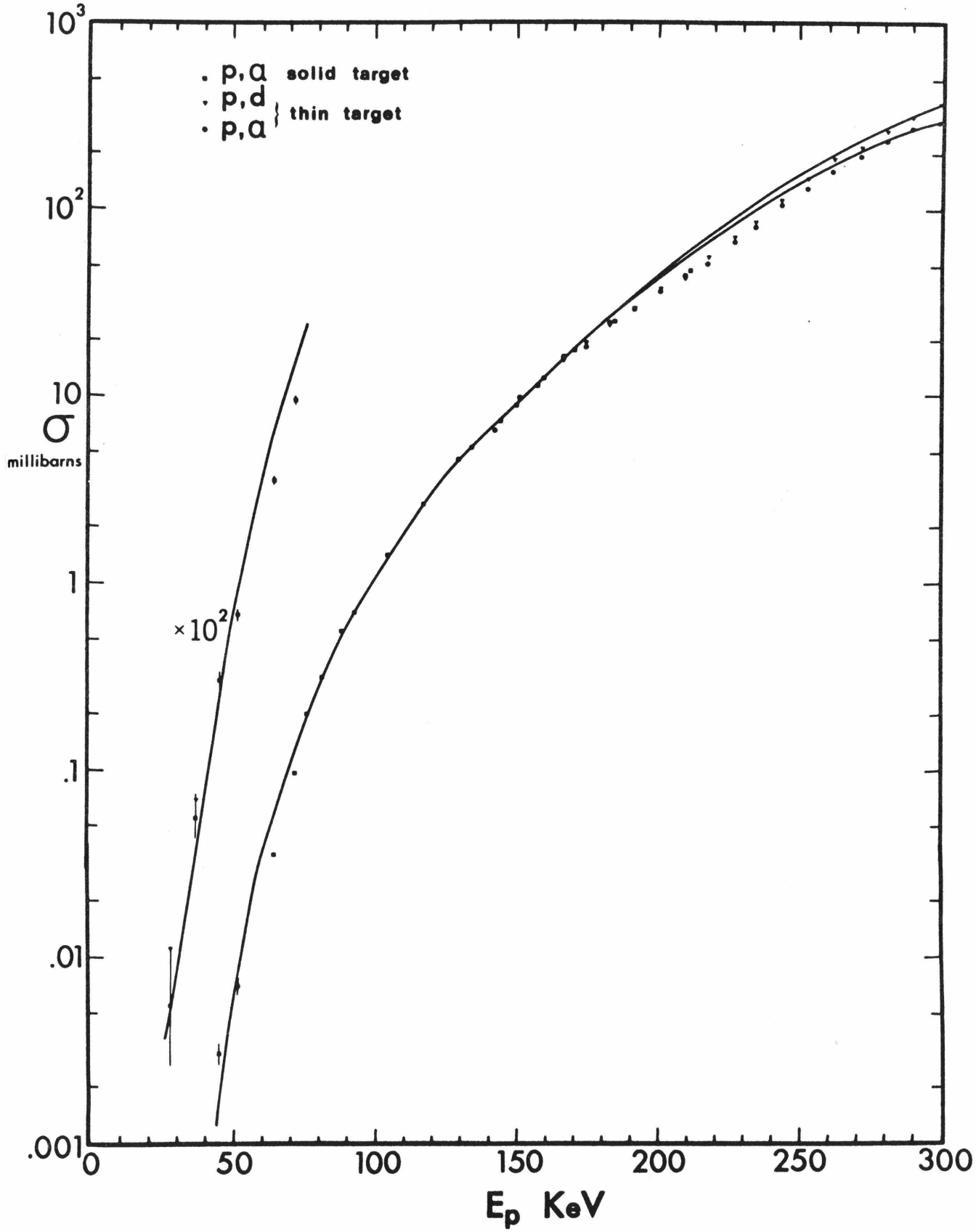
. p, α solid target
. p, d
. p, α thin target
× 10²
10³
10²
10
1
.1
.01
.001
σ
millibarns
0
50
100
150
200
250
300
E_p KeV

FIGURE 11

Center-of-mass counts multiplied by E^2 for alpha particle elastic scattering from beryllium at $\theta_{lab} = 80^{o}$. The horizontal scale is average lab energy in the target layer. See page 8.

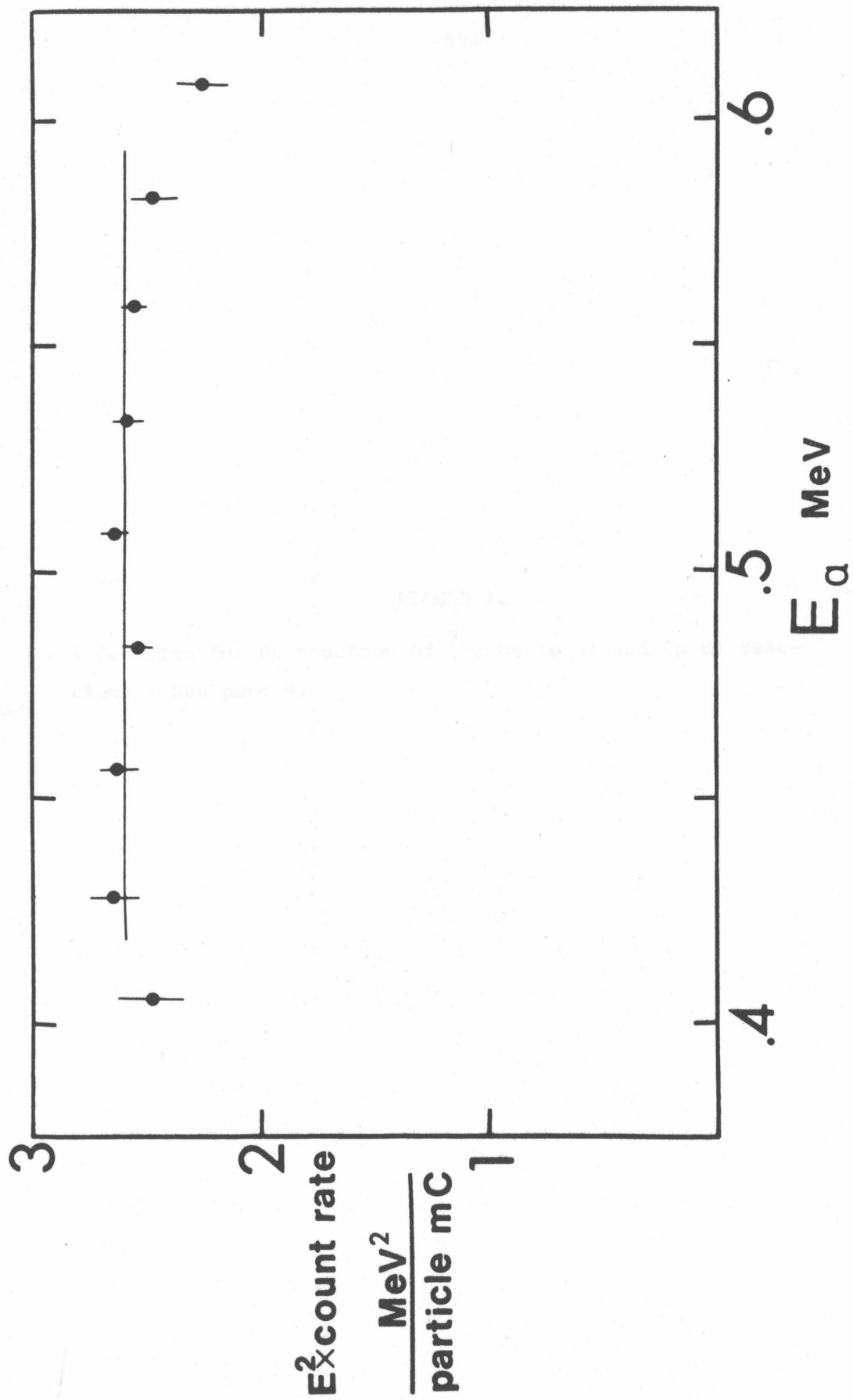
3
2
1
.4
.5
.6
E_α MeV
$E^2 \times$ count rate
$\frac{\text{MeV}^2}{\text{particle mC}}$

FIGURE 12

S function for destruction of ^{9}Be by (p,α) and (p,d) reactions. See page 9.

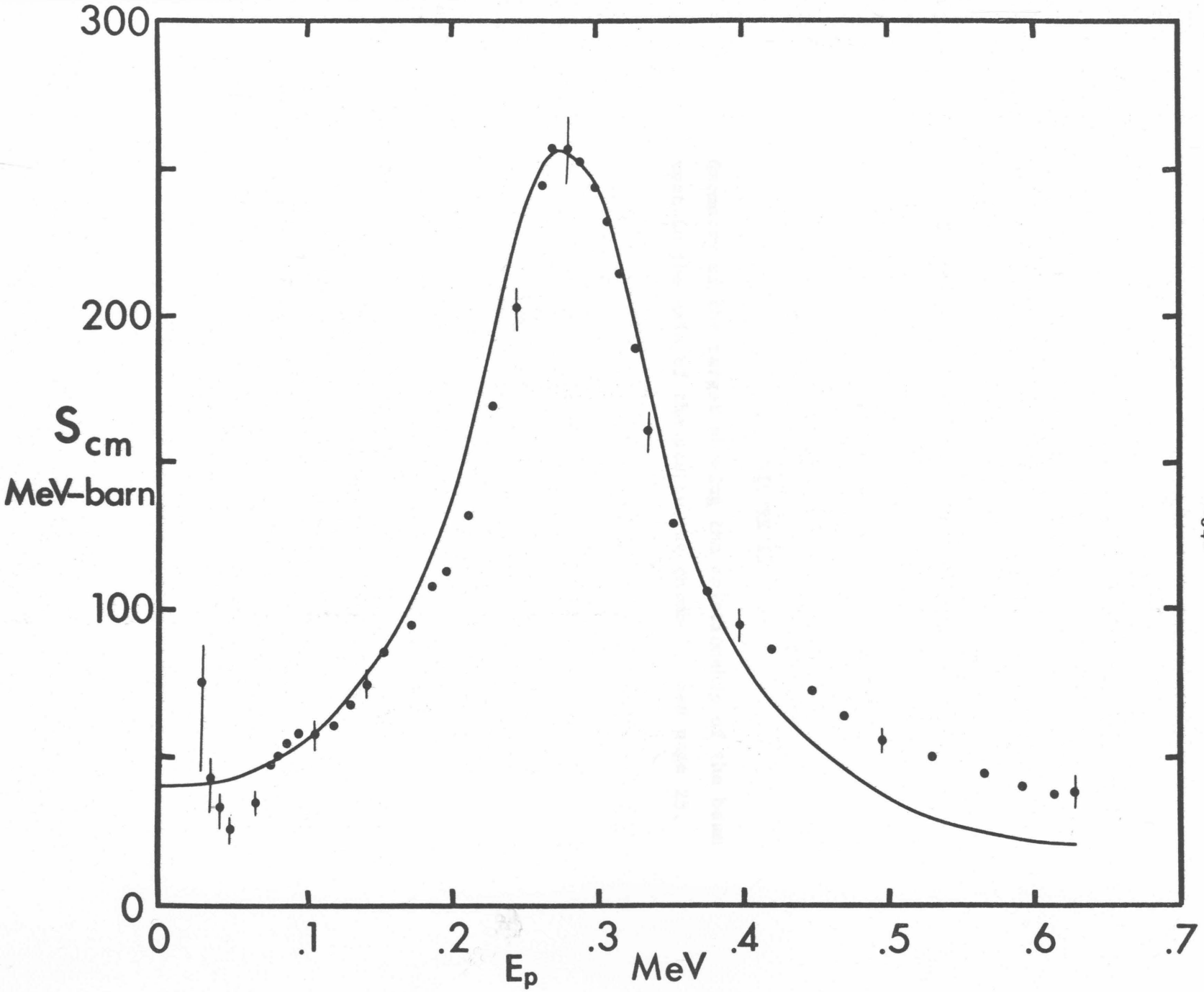
300
200
100
0
S_{cm}
MeV-barn
0
.1
.2
.3
.4
.5
.6
.7
E_p MeV

FIGURE 13

Geometry of the target showing the relationship of the beam spot to the axis of the scattering chamber. See page 25.

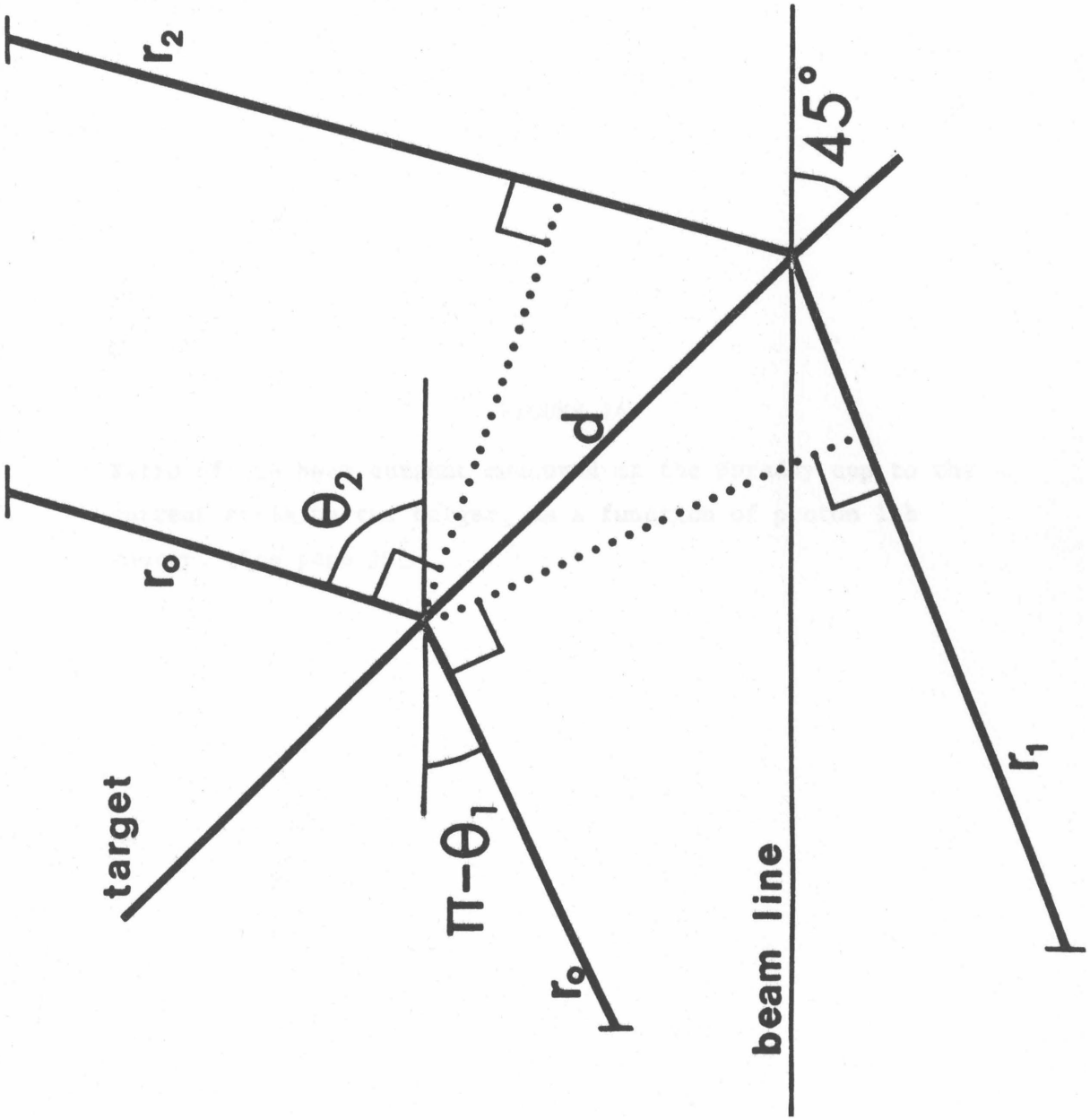
r2
45°
θ2
r0
d
target
π-θ1
r0
beam line
r1

FIGURE 14

Ratio of the beam current measured at the Faraday cup to the current striking the target, as a function of proton lab energy. See page 26.

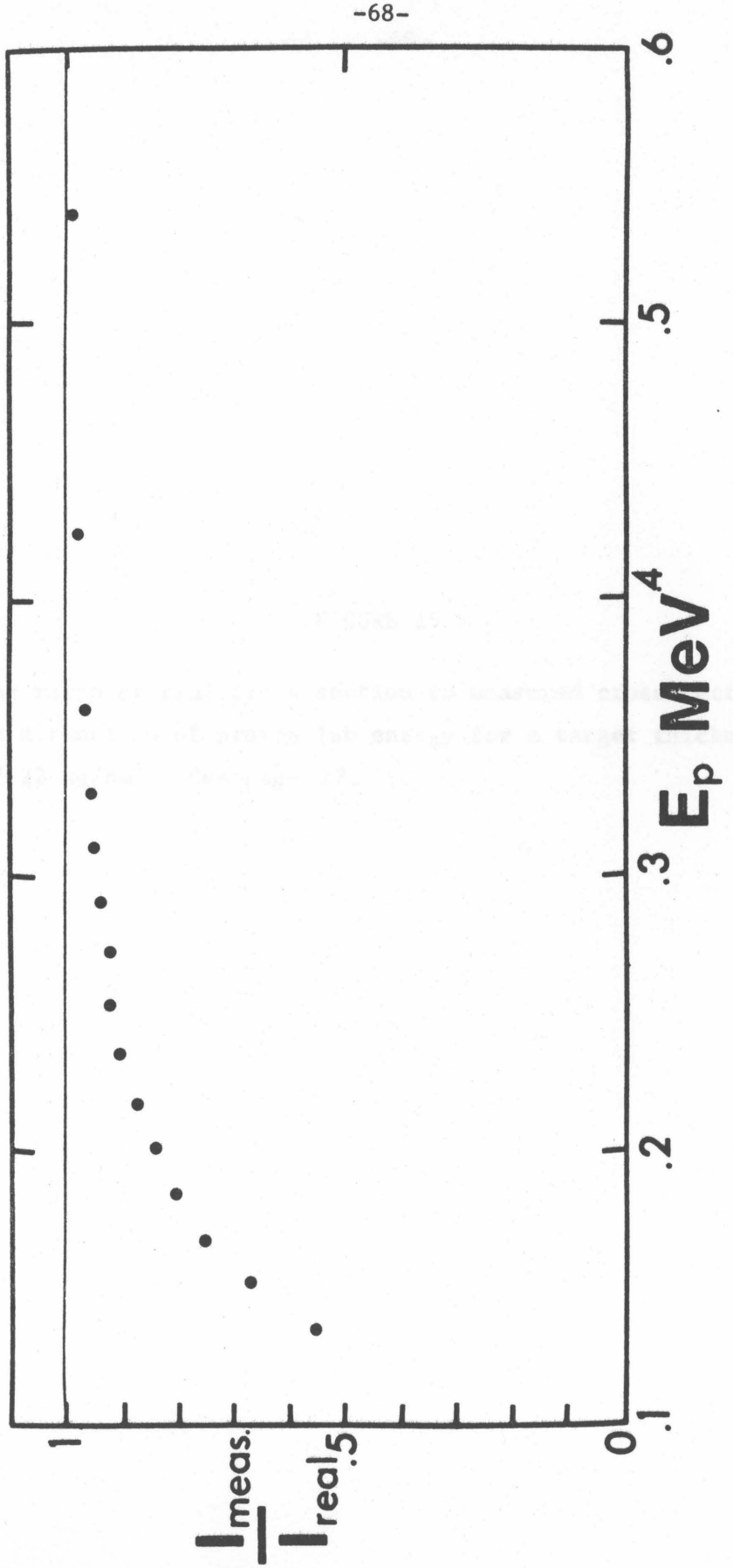
1
0
.1
.2
.3
.4
.5
.6
E_p MeV
$\frac{I_{meas.}}{I_{real}}$
.5

FIGURE 15

The ratio of real cross section to measured cross section as a function of proton lab energy for a target thickness of 22 $\mu g/cm^2$. See page 27.

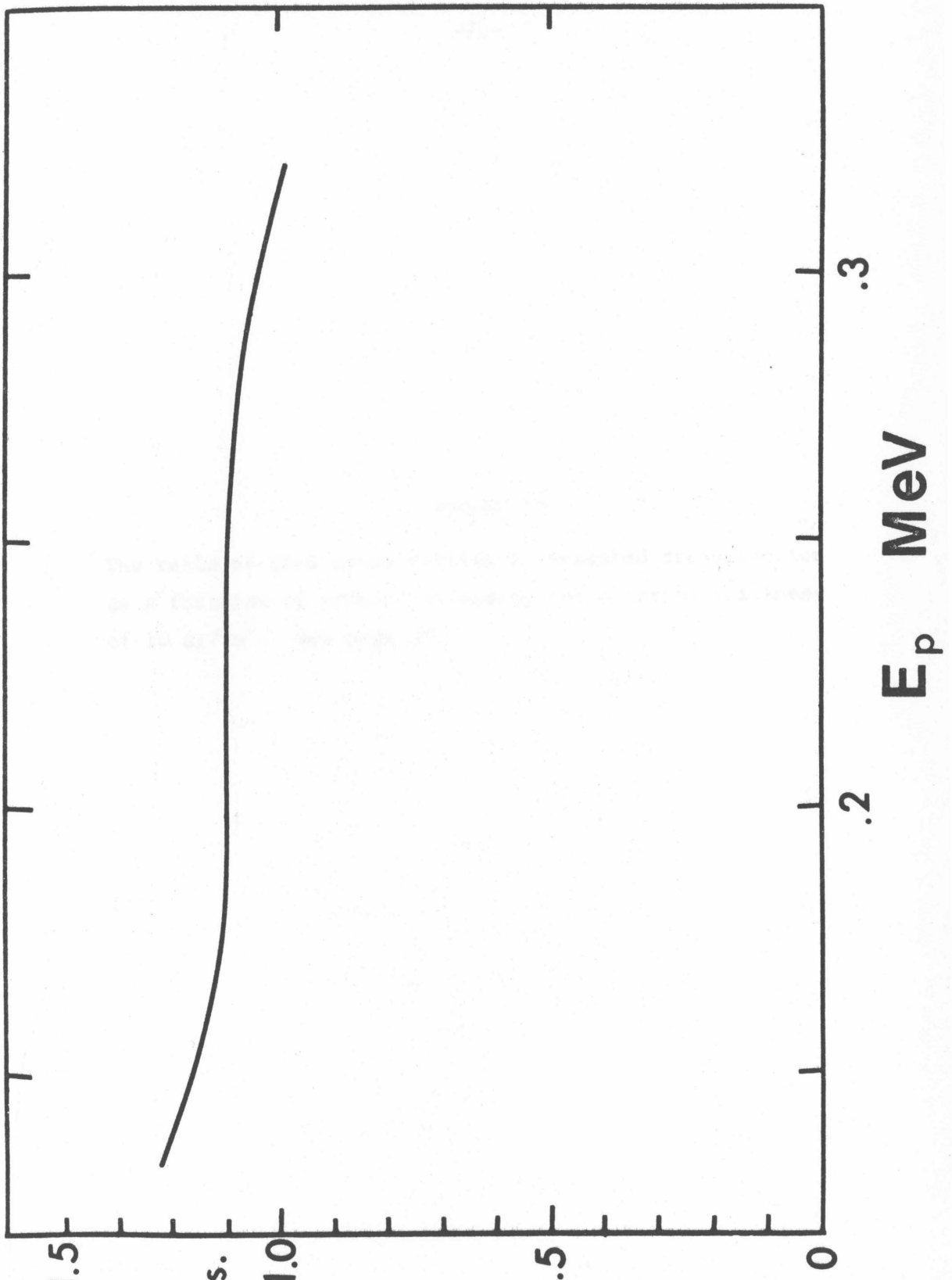
1.5
1.0
.5
0
.2
.3
E_p MeV
$\frac{\sigma_{real}}{\sigma_{meas.}}$

FIGURE 16

The ratio of real cross section to measured cross section as a function of proton lab energy for a target thickness of 10 $\mu g/cm^2$. See page 27.

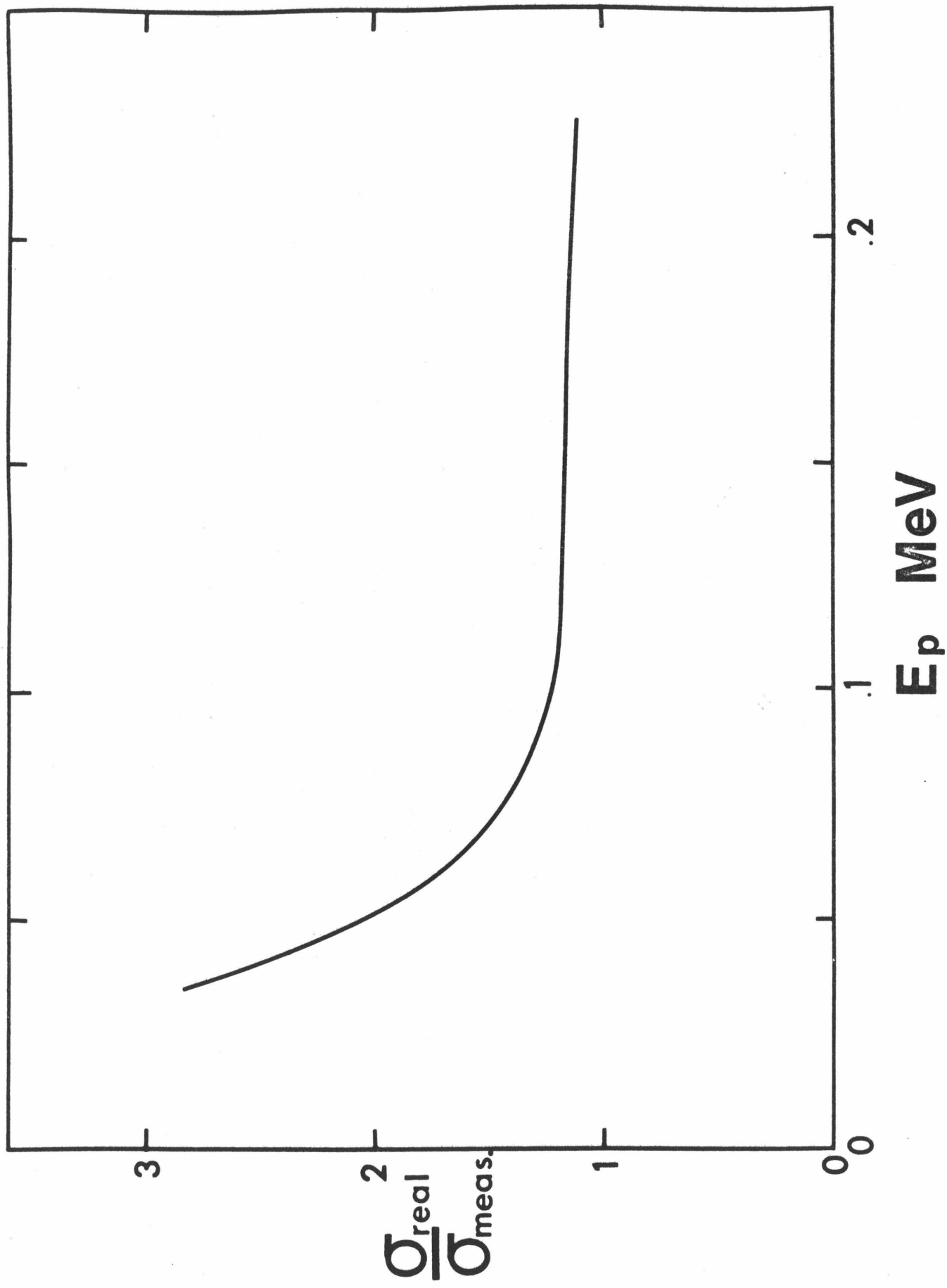
$\sigma_{real}/\sigma_{meas.}$
3
2
1
0
0
.1
.2
E_p MeV